Graduate School Form
30 Updated 12/26/2015

PURDUE UNIVERSITY
GRADUATE SCHOOL
Thesis/Dissertation Acceptance

This is to certify that the thesis/dissertation prepared

By Jeonghwan Kim

Entitled

HIGH EXTINCTION RATIO SUBWAVELENGTH 1D INFRARED POLARIZER BY NANOIMPRINT LITHOGRAPHY

For the degree of Master of Science in Mechanical Engineering

Is approved by the final examining committee:

Jong Eun Ryu
Chair

Likun Zhu

Mangilal Agarwal

To the best of my knowledge and as understood by the student in the Thesis/Dissertation Agreement, Publication Delay, and Certification Disclaimer (Graduate School Form 32), this thesis/dissertation adheres to the provisions of Purdue University's "Policy of Integrity in Research" and the use of copyright material.

Approved by Major Professor(s): Jong Eun Ryu

Approved by: Sohel Anwar 7/27/2016

Head of the Departmental Graduate Program Date

HIGH EXTINCTION RATIO SUBWAVELENGTH 1D INFRARED POLARIZER BY NANOIMPRINT LITHOGRAPHY

A Thesis

Submitted to the Faculty

of

Purdue University

by

Jeonghwan Kim

In Partial Fulfillment of the

Requirements for the Degree

of

Master of Science in Mechnical Engineering

August 2016

Purdue University

Indianapolis, Indiana

Dedicated to my mentors.

ACKNOWLEDGMENTS

First, I would like to thank Professor Jong Eun Ryu for his guidance and advice. This thesis would not have been possible without the contribution and effort of him. I also appreciate Professor Likun Zhu, Professor Mangilal Agarwal for serving as my committee members and for their professional suggestion to my study. I want to thank Dr. Zahyun Ku and Dr. Il Woong Jung. They have been great mentors with their professional knowledge and willingness to help me. I also want to thank all of group members and friends. Most of all, I would like to thank my beloved wife, Suyeon Ko, for her love and patience. I am also forever grateful to my parents, sisters, and the family of Suyeon for their support.

TABLE OF CONTENTS

Page

LIST OF TABLES

LIST OF FIGURES

Figure Page

ABSTRACT

Kim, Jeonghwan. M.S.M.E., Purdue University, August 2016. High Extinction Ratio Subwavelength 1D Infrared Polarizer by Nanoimprint Lithography. Major Professor: Jong Eun Ryu.

Infrared (IR) polarizers have been widely used in military and commercial applications. Controlling the polarization of incident light is one of major issues in the detector systems. However, conventional polarimetric IR detectors require series of polarizers and optical components, which increase the volume and weight of the system. In this research, stacked 1-dimensional (1-D) subwavelength grating structures were studied to develop compact size IR polarimetric detector by using surface plasmonic polariton. Experimental parameters were optimized by Finite Difference Time Domain (FDTD) simulation. Effects of gold (Au) grating size, numbers of stacked gratings, and dielectric space height were tested in the FDTD study. The fabrication of grating layers was conducted by using nanoimprint lithography. The samples were characterized by scanning electron microscopy. IR transmissions in transverse magnetic (TM) and transverse electric (TE) modes were measured by Fourier transform infrared spectroscopy (FTIR).

1. INTRODUCTION

Infrared (IR) detection is been used in a variety of imaging applications from non-invasive medical diagnostics to industrial and military applications such as night vision, overhead intelligence system, and thermal track and search [1, 2]. Mid-IR (3 μm - 8 μm) is particularly interested in military operations since it can be used for identification of ground objects, and air planes and missiles emitting gases. Just as in visible light detection, the IR detectors also have limitations to distinguish hidden objects and to see through the foggy space. Polarimetry is a remedy to resolve those limitations by detecting specific polarization, which is a characteristic of reflected or emitted IR light from the surfaces. Recently, 1-dimensional (1-D) gratings are directly fabricated on IR detection devices to achieve the system-level integration in compact size and lightweight. In this thesis, novel configurations of 1-D gratings are designed and experimentally characterized in order to enhance the performance of polarimetric IR detection.

1.1 Infrared and Detection Methods

Infrared radiation was first discovered by Frederick William Herschel, a British astronomer of German origin in 1800 [3]. Herschel found the temperature of thermometer was increased even though the thermometer is placed outside of red spectrum of sunlight that passed through a prism. In Figure 1.1, IR is placed between visible light and microwaves crossing broad range of 0.74 μm to 1000 μm. IR is generally divided into near infrared (NIR), short wavelength infrared (SWIR), mid wavelength infrared (MWIR), long wavelength infrared (LWIR), and far infrared (FIR, or very long wave infrared (VLIR)) as shown in Figure 1.1. Objects with temperature higher than 0 K emit IR, whose wavelength is longer with lower temperature, vice versa.

Figure 1.2 shows applications of IR images in night vision, global climate monitoring, and cancer diagnosis.

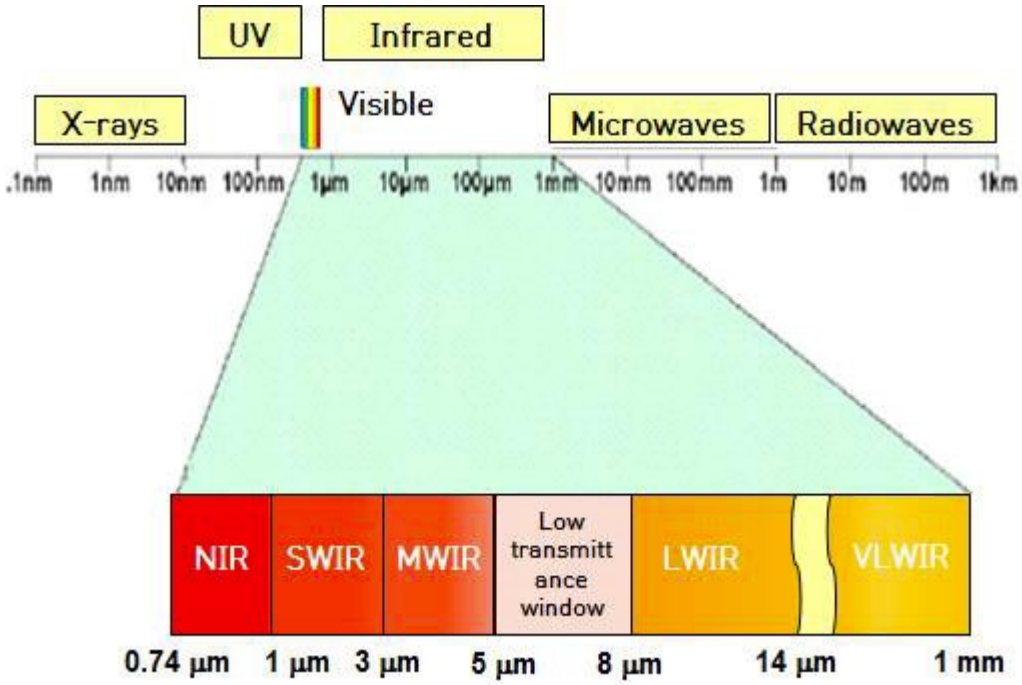

Fig. 1.1. Electromagnetic wave of IR

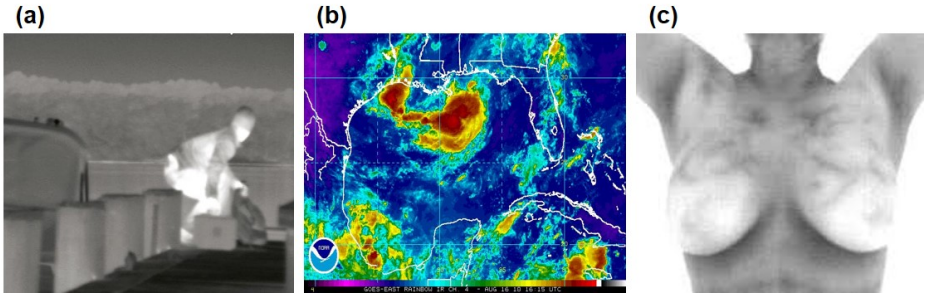

Fig. 1.2. Applications of IR imaging in (a) security night vision camera, (b) climate monitoring, and (c) early detection of cancer

IR detector converts the IR radiation energy to the electrical signal. There are two types of IR detectors: (1) thermal and (2) quantum detectors. In the ther-

mal IR detector, the temperature increase upon the absorption of IR irradiation associates with measurable physical property changes (e.g. thermal expansion, resistance). While the thermal detector is relatively cheap technology and operated in room temperature, it has low sensitivity and slow response time. On the other hand, the quantum detector type, where the irradiated IR excites electrons in the semiconductor layers to generate electrical signals, shows fast response time and high IR sensitivity. Currently, IR detectors based on HgCdTe (MCT), a II-VI semiconductor compound, and InSb, a III-V semiconductor compound, are widely used in commercial market. Semiconductor-based quantum detectors can be packaged into focal plane array (FPA) for high resolution IR imaging. IR FPA has evolved from the single pixel device, to linear array, 2D arrays, and large pixel (4 x 4 K) imagers [2, 4].

1.2 Polarimetric IR Detectors

When the object to detect has insignificant temperature difference from the environment, conventional IR imaging system generates unclear and low-contrast images as shown in Figure 1.3a. On the other hand, polarimetric imaging systems distinguish the polarization of reflected or emitted IR lights, which contains more useful information such as material types and surface roughness, as shown in Figure 1.3b [4–7]. There are non-monolithically and monolithically integrated polarization systems (Figure 1.4). Non-monolithic integrated system uses peripheral optics such as rotating polarizer wheel and retarder in front of the IR FPA. Those extra polarization components cause misalignment errors with the IR FPA, heavy weight, and large volume. On the other hand, the monolithically fabricated 1-D gratings on IR FPA eliminate the misalignment and cumbersome optical components as shown in Figure 1.4b [9–11].

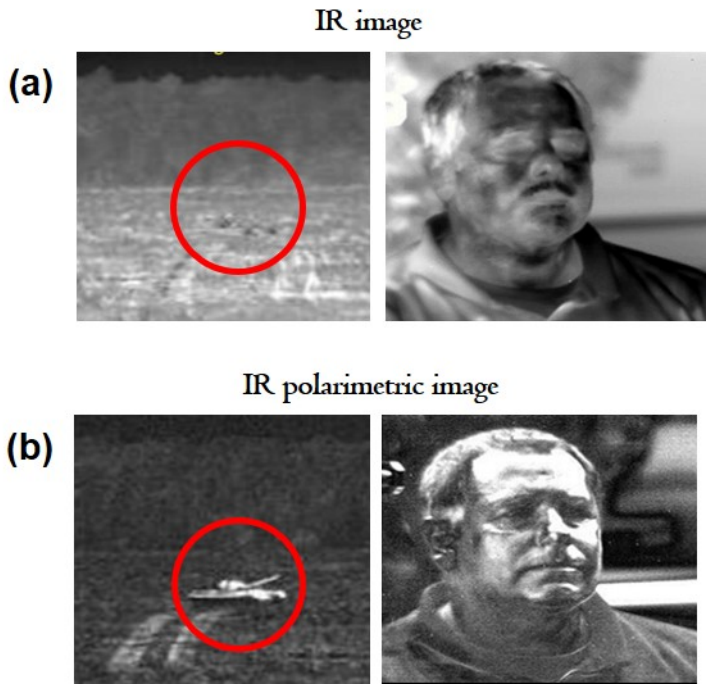

Fig. 1.3. IR imaging system (a) IR image and (b) IR polarimetric image [8]

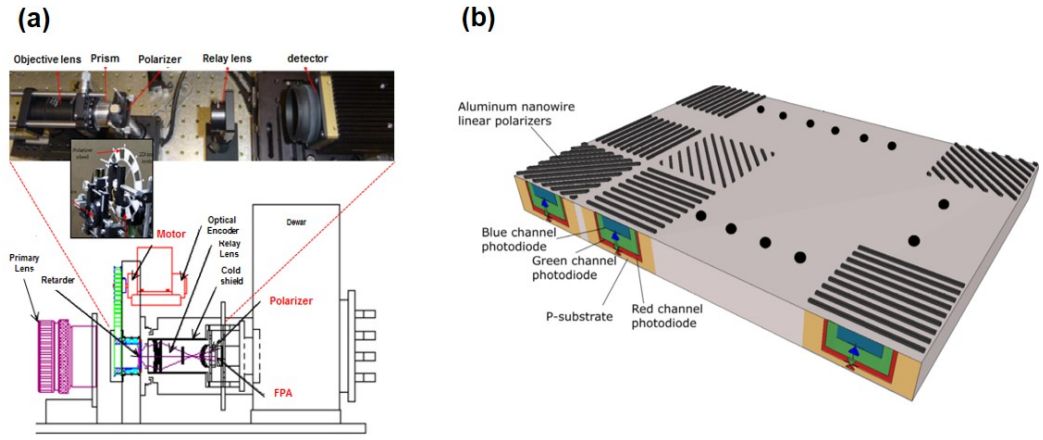

Fig. 1.4. Polarization system (a) non-monolithic integrated system and (b) monolithically integrated polarization systems

1.3 Goal of Thesis

The ultimate goal of this research is to develop a lightweight compact infra-red (IR) imager with polarimetric capability using plasmonic structure coupled focal plane

array (FPA), which consists of photoelectronic detector pixels, possesses fast response time and sensitivity, as shown in Figure 1.5 [2, 4].

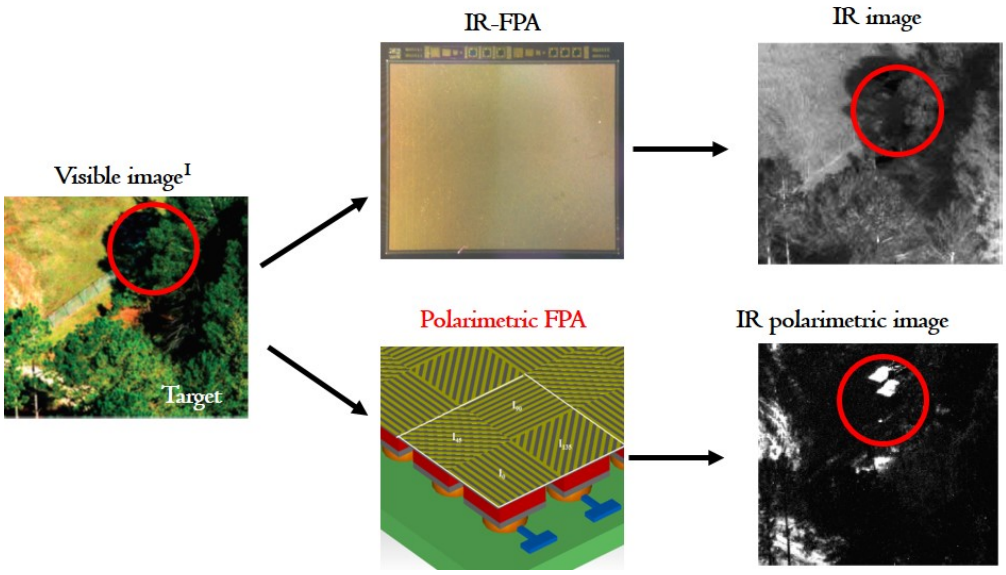

Fig. 1.5. Plasmonic structure coupled focal plane array (FPA) applied polarimetic imager

In this basic study, we designed and experimentally tested double stacked 1-D grating layers with dielectric spacer to enhance the polarimetry characteristics, including transmission and extinction ratio.

As mentioned, the polarizers and retarders are conventionally used to select the light polarization [5,12]. However, such large volume and complexity of those peripheral optical systems have been the major technical barriers in many application areas, where small volume and lightweight are necessary. Successful outcomes of this project will lead to development of polarimetric IR imagers without filtering optics that holds the possibility of greatly improved detection of hard-to-find targets, avoiding the size, complexity and signal-to-noise limitations of existing IR imaging systems.

2. BACKGROUND

2.1 Polarization

Polarization is a property of electromagnetic wave that can oscillate in specific directions. Of note, electromagnetic wave consists of electric and magnetic fields, which are perpendicular each other, and polarization of light refers to the direction of electric fields. The polarization of light is also affected by the light matter interaction [13]. Equation 2.1 describes x and y components of electric field propagating in z direction.

$$\begin{aligned} E_x(z,t) &= iE_{0x}cos(kz-\omega t) \\ E_x(z,t) &= iE_{0y}cos(kz-\omega t+\phi) \end{aligned} \tag{2.1}$$

As shown in Figure 2.1a, it is defined as linear polarization when the projected electric field on the xy plane is a straight line, which occurs with $\phi = 2\pi n$ (n=0, 1, 2, $\cdots$). On the other hand, the projected electric field rotates in circular direction (Figure 2.1b) when the phase difference in x and y components is $\pi/2$. Elliptical polarization (Figure 2.1c) refers to the electric fields rotates while changing the amplitude.

2.2 Surface Plasmon

Plasmon effect is the collective oscillations of electrons interacting with specific electromagnetic wavelength, and the use of surface plasmon structures for wavelength filtration and polarization has attracted growing interest in the IR sensing and imaging [4, 14]. There are four main reasons why integration of the plasmonic nanostructures with FPA is a promising approach to the next generation polarimetric IR imagers. First, the filtering wavelength can be readily tuned by geometric modification of the filter. Second, the plasmonic structures can incorporate enhanced polarization

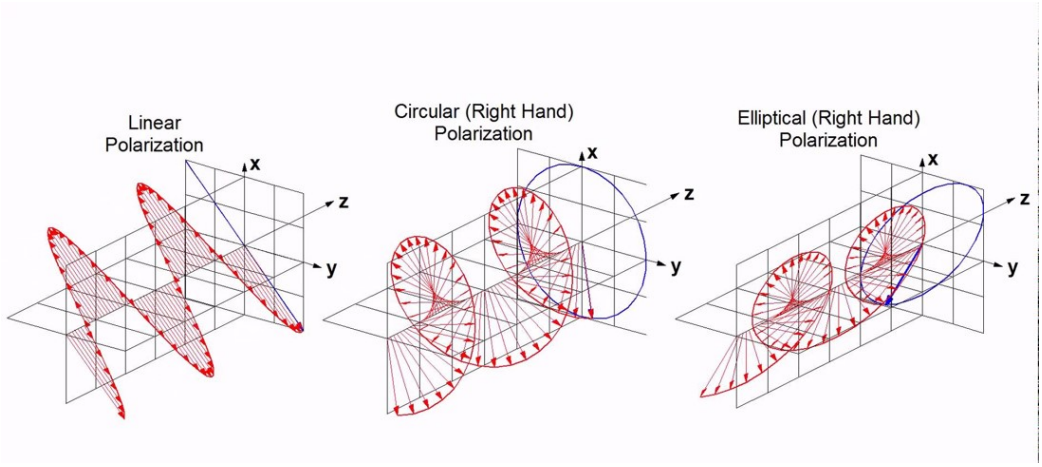

Fig. 2.1. Different types of polarization (a) Linear polarization, (b) Circular polarization, and (c) Elliptical polarization

sensitivity (i.e. extinction ratio) into detectors. Third, the amplification of electromagnetic near-fields can be exploited for enhanced absorption and photocurrent. Finally, plasmonic structures, which are nanoscale thin films, can be monolithically fabricated directly on FPAs with negligible addition of weight and volume [4].

Surface plasmon polariton (SPP) is an oscillation of free electrons in the metal surface, and the SP dispersion relation by Maxwell's equation, which is the frequency dependent SP wave vector (k_{spp}), shows:

$$k_{spp} = k_0 \sqrt{\frac{\varepsilon_d \varepsilon_m}{\varepsilon_d + \varepsilon_m}} \tag{2.2}$$

where k_0, ε_d, and ε_m are the free space wave vector, and frequency dependent permittivity of dielectric material and metal, respectively. Since k_{spp} is greater than k_0, the momentum mismatch must be compensated to generate SP [15]. Therefore, the SP wave vector matches the momentum difference by adding a reciprocal wave vector, $G = i2\pi/p$, and an incident angle (θ) as shown in Equation 2.3:

$$k_{spp} = k_0 sin\theta x + \frac{i2\pi}{p} x \tag{2.3}$$

where i and p are integer and pitch of metal grating. When the incident angle (θ) is zero, i.e. normal incident light, the wavelength of SPP is:

$$\begin{aligned} |k_{spp}| &= \frac{i2\pi}{p} \\ \lambda_{spp} &= \frac{2\pi np}{i2\pi} = \frac{np}{i} \end{aligned} \tag{2.4}$$

where n is the refractive index of the dielectric material. Therefore, the first and k-th SPP resonance occur at $\lambda_{spp} = np$ and $\lambda_{spp} = np/k$, respectively.

2.3 Finite Difference Time Domain (FDTD) Simulation

Preliminary FDTD simulation study was conducted with CST Microwave Studio. Figure 2.2a shows single subwavelength grating made of 1-D gold (Au) wires on a Silicon (Si) substrate. The x and y axes are perpendicular and parallel to the 1-D Au gratings, respectively. The incident light is parallel to the z axis. Two types of linear polarized lights are tested: TM (Transvers Magnetic) and TE (Transvers Electric), which are perpendicular and parallel to the 1-D subwavelength grating, respectively. p_1, w_1, and t_{Au1} are pitch, width, and thickness of the 1-D grating, respectively. For the double-stacked 1-D grating design, benzocyclobutene (BCB) dielectric spacer was coated on the Si substrate (Figure 2.2b). The Au gratings on the bottom and top layers are aligned in the simulation. $p_2, w_2, t_{Au2}, t_{BCB}$ are the pitch, width, thickness of the second Au grating, and the thickness of BCB, respectively. In the simulation study, $p = p_1 = p_2, w = w_1 = w_2$ and $t_{Au} = t_{Au1} = t_{Au2}$ are used.

Figure 2.3 shows the trends of TM transmission, TE transmission, and extinction ratio ($R_2 = \int T_{TM} \cdot d\lambda / \int T_{TE} \cdot d\lambda$) of single and double-stacked 1-D gratings. In Figure 2.3 (a-c), the pitch (p) is changed from 0.3 μm to 1.2 μm with 0.1 μm step and fixed width/pitch ratio (r) of 0.7. Figure 2.3 (d-f) show the transmissions and extinction ratio with $p = 0.4$ and various $r = 0.3$, 0.4, 0.5, 0.6, 0.7, 0.8, and 0.9. For those simulation, the thickness of Au was fixed to 0.1 μm. While TE transmission is suppressed, TM transmission and extinction ratio are improved as the pitch

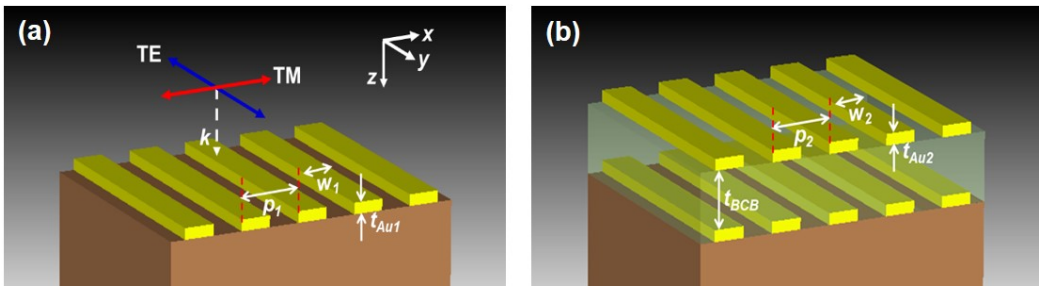

Fig. 2.2. Schematic views of (a) single 1-D subwavelength grating and (b) stacked 1D subwavelength grating on a Si substrate

(p) decreases. The simulation results in Figure 2.3a confirm that the SPP wavelength (λ_{spp}) shifts to the longer wavelength when the pitch increases as predicted in Equation 2.4. On the other hand, as shown in Figure 2.3 (d-f), the TM and TE transmissions increase while the extinction ratio shows downward trend with smaller grating width/pitch ratio (r).

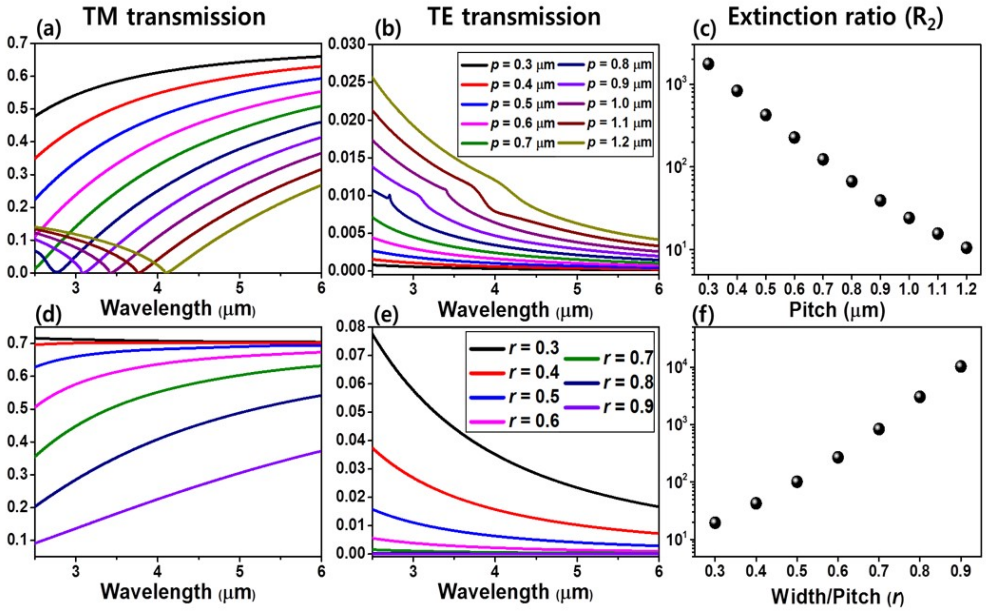

Fig. 2.3. Trends of TM transmission, TE transmission, and extinction ratio

Influence of BCB thickness (t_{BCB}) on the extinction ratio of double-stacked 1-D gratings with $p = 0.4\ \mu m$, $0.7\ \mu m$ and $1.0\ \mu m$ are shown in Figure 2.4. BCB thickness

(t_{BCB}) was changed from 0.05 μm to 0.85 μm with a step of 0.20 μm. r ($= w/p$) and (t_{Au}) were fixed at 0.7 and 0.1 μm, respectively. Simulated extinction ratio of the double stacked grating is higher than the single-layered grating for the all pitches (p). The simulation shows the extinction ratio increases up to $t_{BCB} = 0.45$ μm then decreases again.

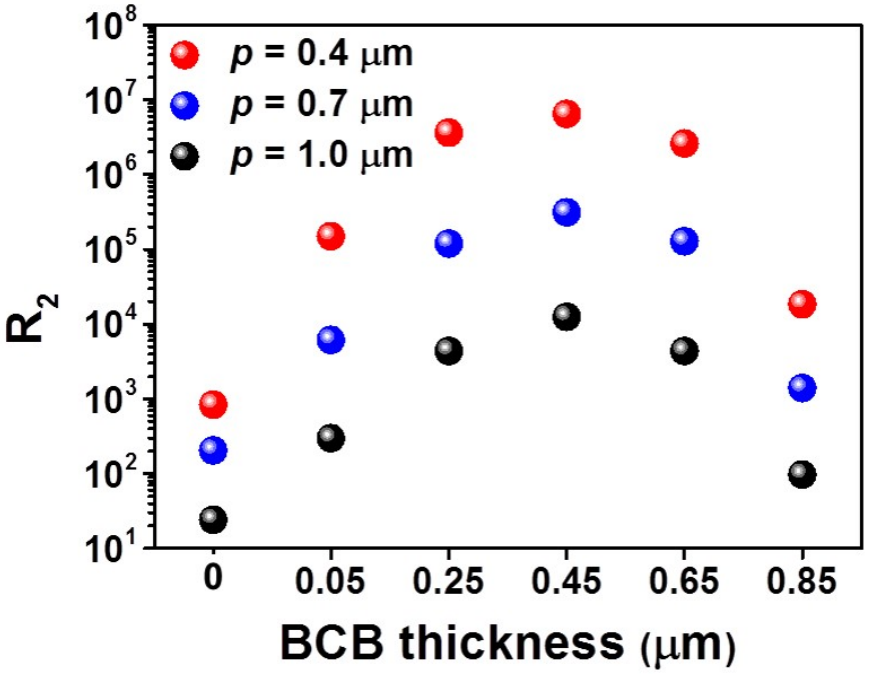

Fig. 2.4. Influence of BCB thickness (t_{BCB}) on the extinction ratio of double-stacked 1-D gratings

3. MATERIALS AND APPARATUS

3.1 Nanoimprint Lithography

In nanoimprint lithography (NIL), a stamp with protruded nanoscale patterns is used to physically contact and deform a polymeric layer on a substrate. Figure 3.1 shows schematic diagrams of NIL process.

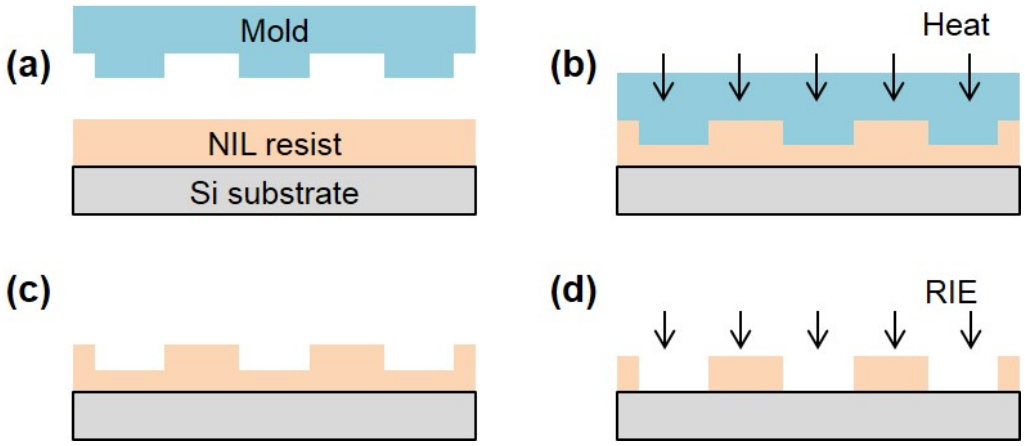

Fig. 3.1. Schematic diagrams of thermal NIL process

There are two types of NILs depending on the polymeric resist materials: 1) Thermal NIL using thermoplastic resist and 2) Ultraviolet (UV) NIL using UV curable resist. For the thermal NIL, the resist is heated above its glass transition temperature. Then, a large pressure (500 - 1000 psi) is applied to the mold that is placed on the heated resist to fill the spaces on the mold (Figure 3.1b). Upon cooling, the mold is removed, and the resist is permanently deformed as shown in Figure 3.1c. The residual layer, which is the area under the protrusions on the mold, can be removed by a anisotropic plasma etch to expose the surface of Si wafer and to leave the resist for following fabrication processes, such as metal deposition lift off or Si

etching (Figure 3.1d). The cost of thermal NIL is lower than any other nanoscale lithography technology due to simple equipment set up. However, high temperatures and pressures involved in the process can cause distortions induced misalignment. Moreover, the thermal expansion coefficient mismatch between the polymeric resist and Si wafer lead to residual stress during cooling [16].

On the other hand, UV NIL that is a room temperature process and uses low pressure eliminates the temperature induced misalignment and residual stress. Given the advantages, UV NIL is a superior choice of for many applications including this study. It requires a pattern transfer layer (bottom) and UV curable resist layer (top) as shown in Figure 3.2a. The transfer layer is required since the resist is not easily dissolvable in organic solvents. Polymethyl methacrylate (PMMA) is generally used as the transfer layer. Low viscosity UV NIL resist is used so that the uncured polymer can easily fill the space on mold with low pressure. In order to cure the UV resist, the NIL mold should be made of UV transparent materials. Instead of heat, the deformed resist layer is cured by UV as shown in Figure 3.2b. After the mold is removed, the residual UV resist and the transfer layer are anisotropic etched with RIE (Figure 3.2c, d).

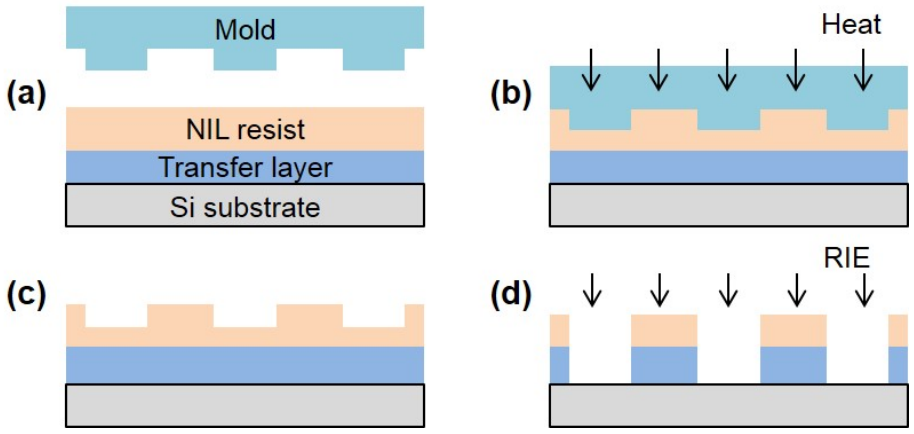

Fig. 3.2. Schematic diagrams of UV NIL process

3.2 UV NIL Materials

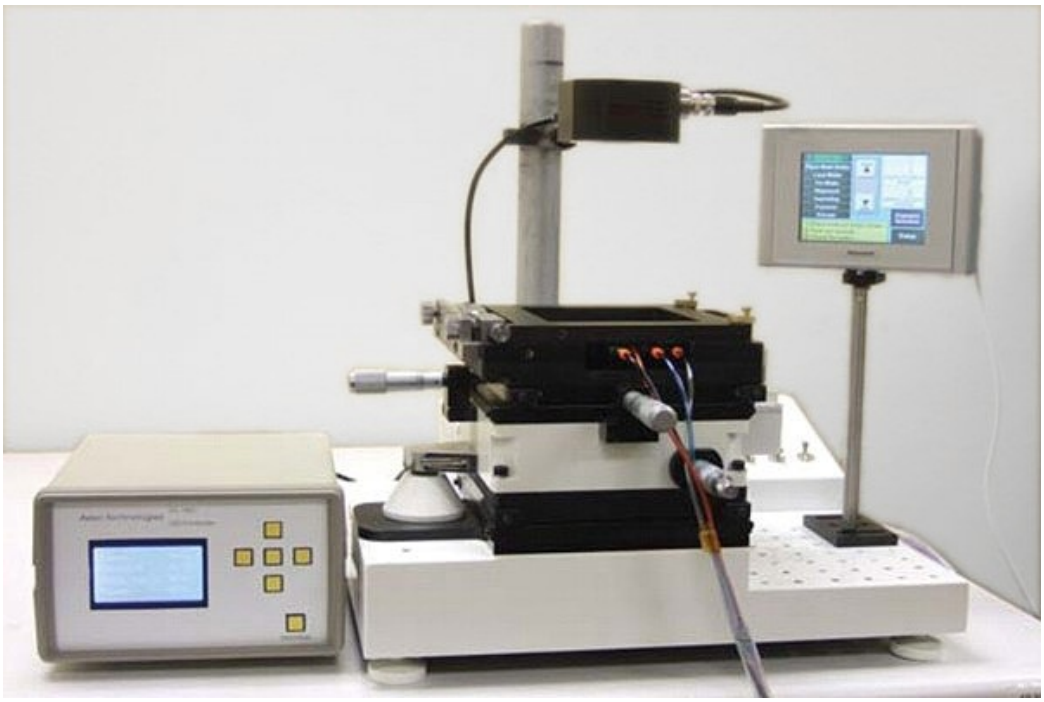

Fig. 3.3. Nanoimprint lithography equipment, PL-400

A commercial NIL machine (EZimprinting Inc., PL-400, Figure 3.3) was used during the course of this work. In this thesis work, PMMA was chosen due to its solubility in acetone for the metal lift-off process, and AR-UVP (EZimprinting Inc.) was used as the UV NIL resist. The UV resist contains a reactive silicon-containing oligomer that cross-links as photo-initiators are activated by UV radiation. The UV resist is resistant to the O_2 plasma and needs fluorocarbon (CF_4 or CHF_3) for RIE.

3.3 Electron Beam Lithography

In electron beam lithography (EBL), focused electron beam is absorbed by electron sensitive resist layer to generate nanoscale range intramolecular phenomena. Since the electron beam directly writes designed patterns on the EBL resist without any masks or reticles, it is considered the most flexible lithography method with high resolution

(< 10 nm). However, the serial writing process is considered to have low productivity and high cost. In this course of study, JEOL JBX-9300FS and PMMA are used as the EBL system and resist, respectively, through the user facility in Argonne National Laboratory.

3.4 Fourier Transform Infrared Spectroscopy

FTIR spectrometer (Nicolet 6700, ThermoFisher Scientific, Figure 3.4) equipped with polarizer and focusing lens was used to measure TM and TE transmission of grating patterned Si substrate.

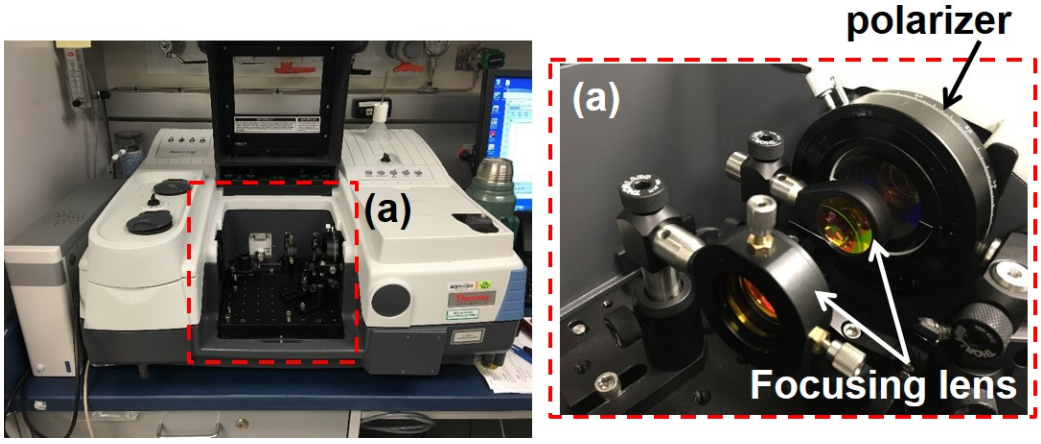

Fig. 3.4. FTIR spectrometer, Nicolet 6700

4. EXPERIMENT PRODECURES

4.1 Design of NIL Patterns

Figure 4.1 shows dimensions of 1-D gratings designed by Tanner L-edit (Mentor Graphics, USA). L-edit is a powerful computer design tool, which creates layouts of Micro-Electro-Mechanical Systems (MEMS) or Integrated Circuits (ICs). Three designs of 1-D gratings were selected: 1) $p = 400$ nm and $w = 280$ nm, 2) $p = 700$ nm and $w = 490$ nm, and 3) $p = 1000$ nm and $w = 700$ nm. The total area of pattern for each design is 5 mm $\times$ 5 mm.

4.2 Mold Fabrication Process

The Si mold fabrication process is summarized in Figure 4.2. The template for nanoimprint mold was fabricated by electron beam lithography (EBL, JEOL JBX-9500FS, USA) at the Argonne National Laboratory (Center for Nanoscale Materials). Positive tones resist, GL-2000 (MicroChem Corp., USA), was used for EBL in this study. EBL resist was dropped on a clean Si wafer and spun with 5000 rpm for 45 sec to make 350 nm of film thickness. The resist coated wafers were baked on a hot plate at 150 $^{\circ}C$ for 1 min. The resist thickness was measured to be 358 nm (F20, Filmetrics). Before the EBL writing process, e-beam was focused to Au nanoparticles on the substrate stage. Then, the focused-electron beam current is measured at 50,000-times magnification with Faraday cup that connected to an external picoammeter. A proper level of e-beam dosage for the resist film was determined through dosage tests. In this study, e-beam dosage for the 350 nm of GL-2000 resist was 325 C. After e-beam writing, the wafer was immersed into Xylene (99 %, MicroChem Corp., USA) for 45 sec for development. The wafer was then rinsed with isopropyl alcohol (IPA).

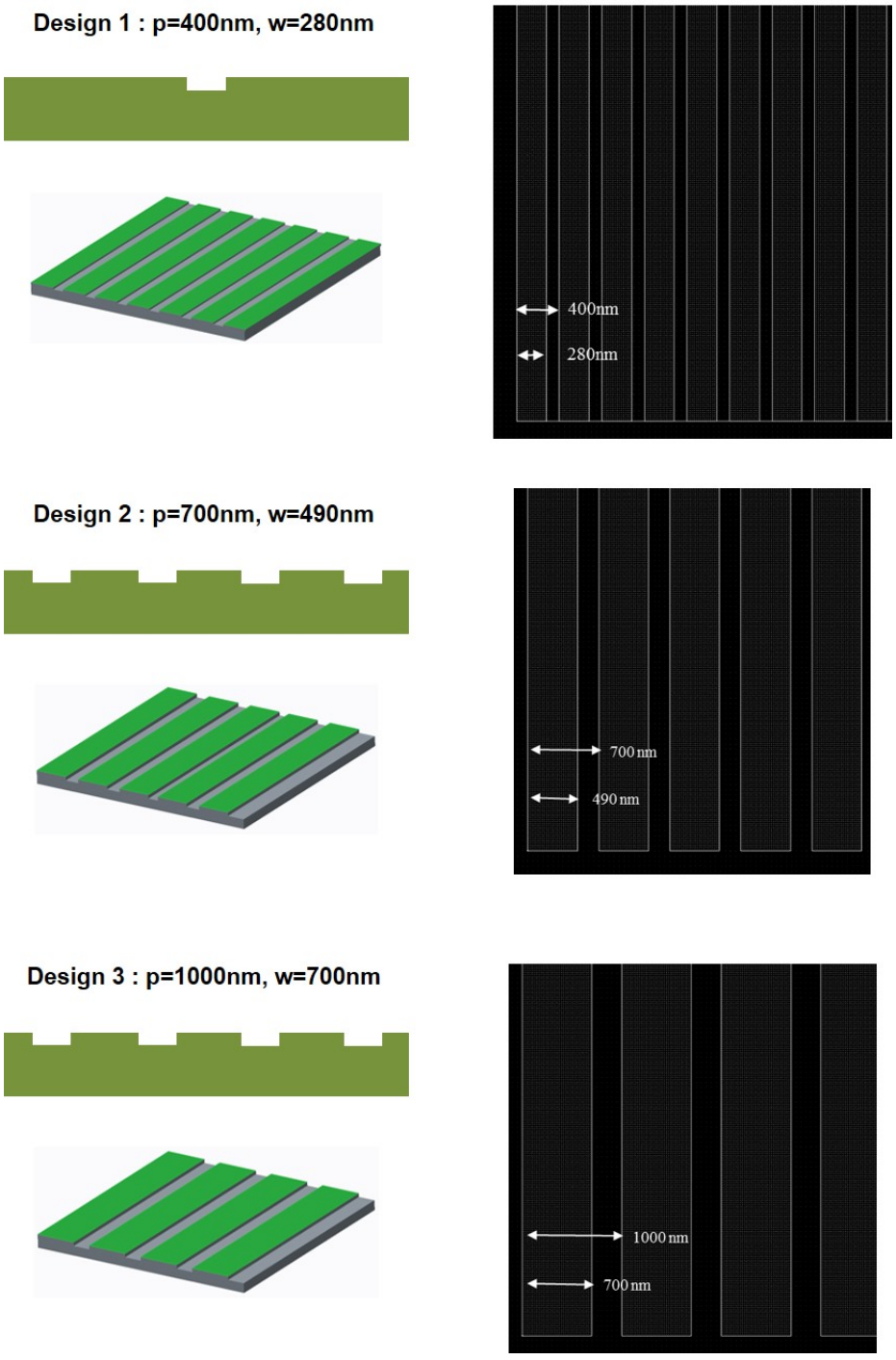

Fig. 4.1. Selected designs of gratings. (a) pitch (p) = 400 nm and grating width (w) = 280 nm; (b) p = 700 nm and w = 490 nm; and (c) p = 1000 nm and w = 700 nm

Oxford Plasmalab System 100 (Center for Nanoscale Materials, Argonne National Laboratory) was used for anisotropic etching of Si with the e-beam resist mask. Mixture of HBr and O_2 gases was used for Si etching with 40 sccm and 8 sccm of flow rates, respectively. Base pressure and RF power were set to 4 mTorr and 200 W, respectively. Under those process condition, calculated etch rate of Si wafer was 2.2 nm/sec. In this study, Si was etched by 200 nm.

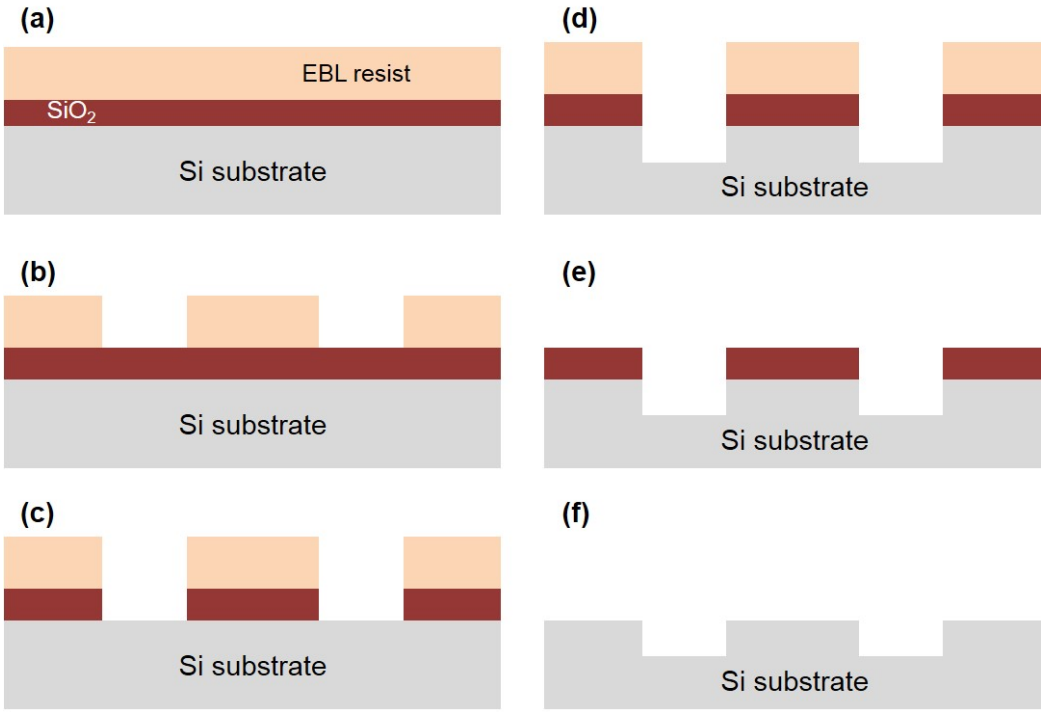

Fig. 4.2. Si mold fabrication process

Process flow for NIL soft mold fabrication is depicted in Figure 4.3. The EBL generated Si mold was hydrophobic treated by using chemical vapor deposition of 1H,1H,2H,2H-perfluorooctyl-trichlorosilane (F13-TCS) in a vacuum desiccator. Polydimethylsiloxane (PDMS, Sylgard 184, Dow Corning) block was used as the substrate of NIL soft mold. In order to improve the adhesion on PDMS, the surface of PDMS was treated with O_2 plasma. Then, a UV curable polymer, Ormostamp (Microchem), was coated on the hydrophobic treated Si mold, and the PDMS block was gently

pressed on the Si mold. The NIL mold polymer (Ormostamp) is cured by a UV lamp ($\lambda = 365$ nm). After the cured NIL mold polymer was cured, the PDMS was peeled off from the Si mold with the cured Ormostamp. The NIL mold was treated with O_2 plasma and hydrophobic chemical vapor deposition.

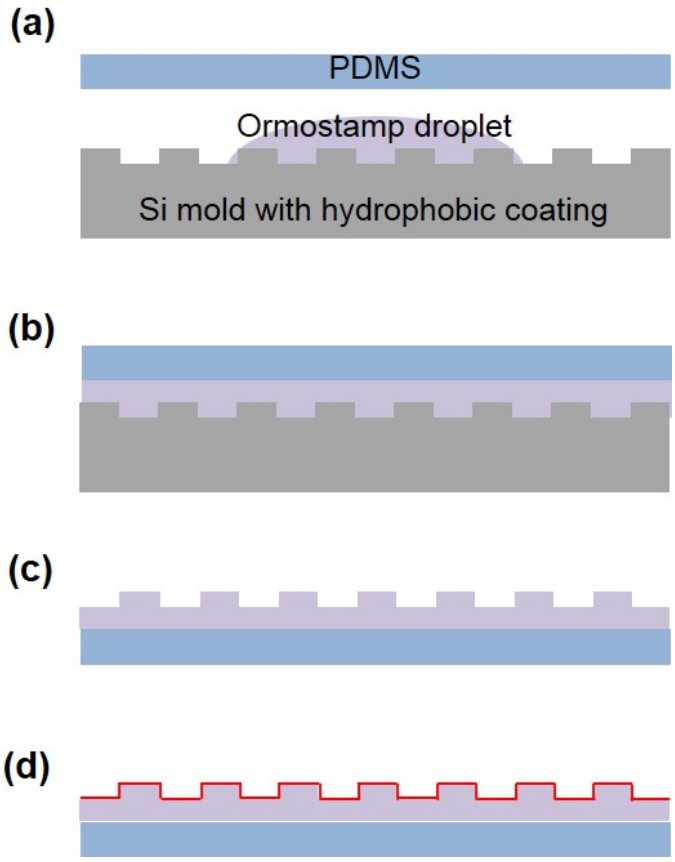

Fig. 4.3. NIL soft mold fabrication process

4.3 Sample Fabrication

NIL was performed with the PL-400 (EZimprinting) as shown in the process flow (Figure 4.4). Double side polished Si substrates were cleaned with acetone, methanol, isopropanol, and rinsed with deionized water. PMMA (transfer layer) of 300 nm thickness was spin coated with 5000 rpm for 20 sec. The wafers were baked on a hot

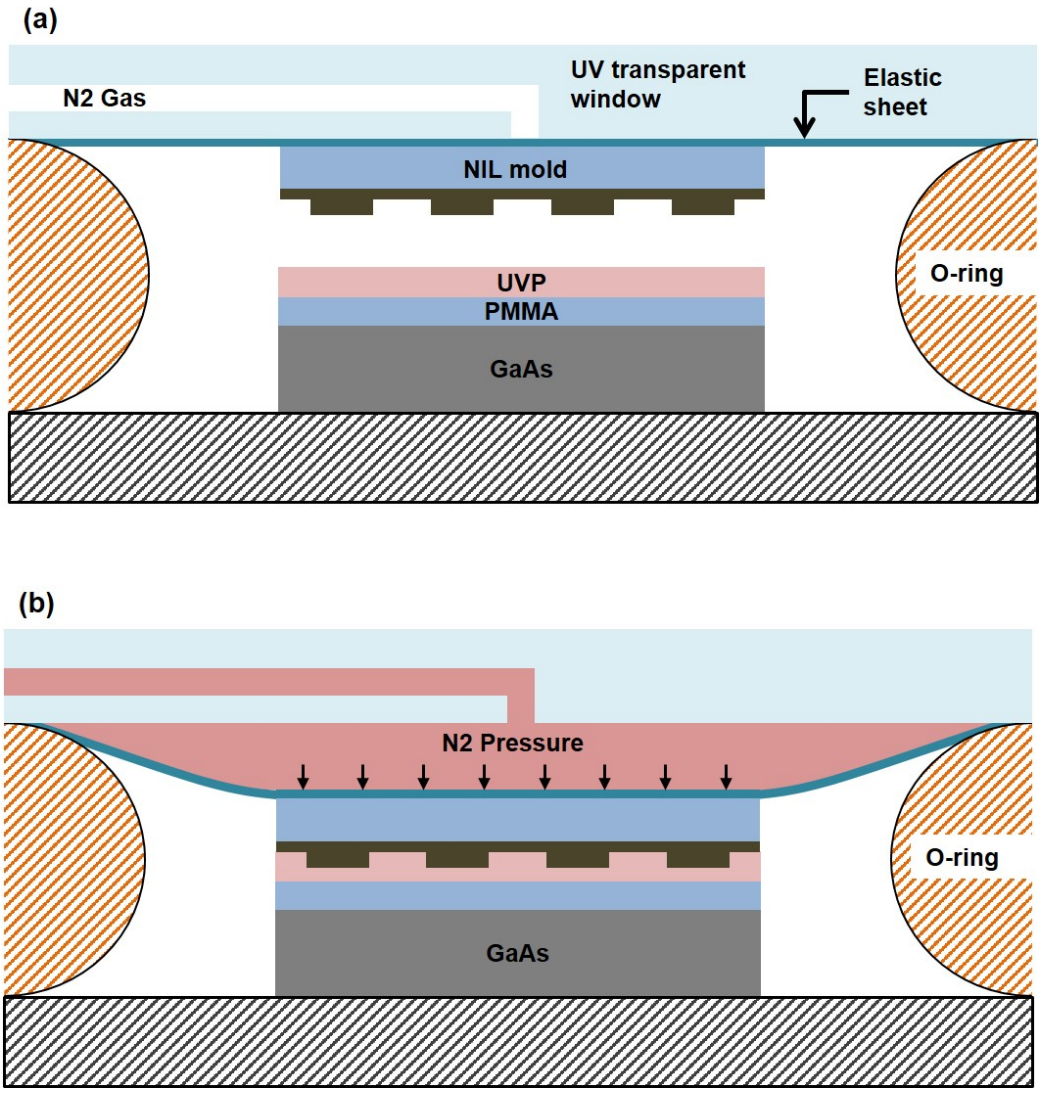

Fig. 4.4. Schematic view of NIL chamber (a) without and (b) with N2 pressure on the backside of NIL mold.

plate (180°C, 2 min) and air cooled slowly. UV NIL resist (UVP, EZimprinting) was spin coated on the PMMA with 3000 rpm for 10 sec. Then, the resist-coated wafers are placed on the sample stage of imprinter. The hydrophobic treated NIL soft mold is also attached on the elastic imprint sheet as shown in Figure 4-4a. The NIL mold and wafer are aligned with the optical microscope. Then, the o-ring is inflated to seal the chamber (Figure 4.4a), and the chamber is evacuated until 10 psi. After 2min of

evacuation at 10 psi, N_2 gas is opened to pressurize the imprint sheet from the top, and the NIL mold is impressed into the NIL resist as shown in Figure 4.4b. The NIL pressure and time used in this experiment are 35 psi and 2 min, respectively.

The NIL resist residual and PMMA transfer layer were anisotropic etched by RIE. The RIE parameters for UVP and PMMA layers are shown in Table 4.1. 100 nm Au thin-film was deposited by electron beam evaporator (Lesker CMS 18) with deposition rate of 12 nm/min followed by acetone lift off for over night. BCB dielectric spacer layer (500 nm) was spin coated on the Au grating patterned wafer. The second Au grating layer was patterned on BCB by the same NIL, RIE, and deposition processes.

Table 4.1
RIE parameters for UVP and PMMA

RIE process		
Resist	**Parameter**	
NIL resist	Gases	CHF_3 (20 sccm), O_2 (2 sccm)
	Base pressure	7 mTorr
	RF / ICP power	75 W
	Etch rate	1.2 nm/sec
PMMA	Gases	O_2 (20 sccm)
	Base pressure	4 mTorr
	RF / ICP power	50 W
	Etch rate	1.5 nm/sec

5. RESULTS AND DISCUSSION

5.1 Si Mold Fabrication with EBL

Figure 5.1 shows the optical images (a-c) and SEM micrographs (d-f) of Si molds. Figures 5.1(a, d), 5.1(b, e), and 5.1(c, f) are the Si molds for p = 400 nm, 700 nm, and 1000 nm 1-D gratings, respectively.

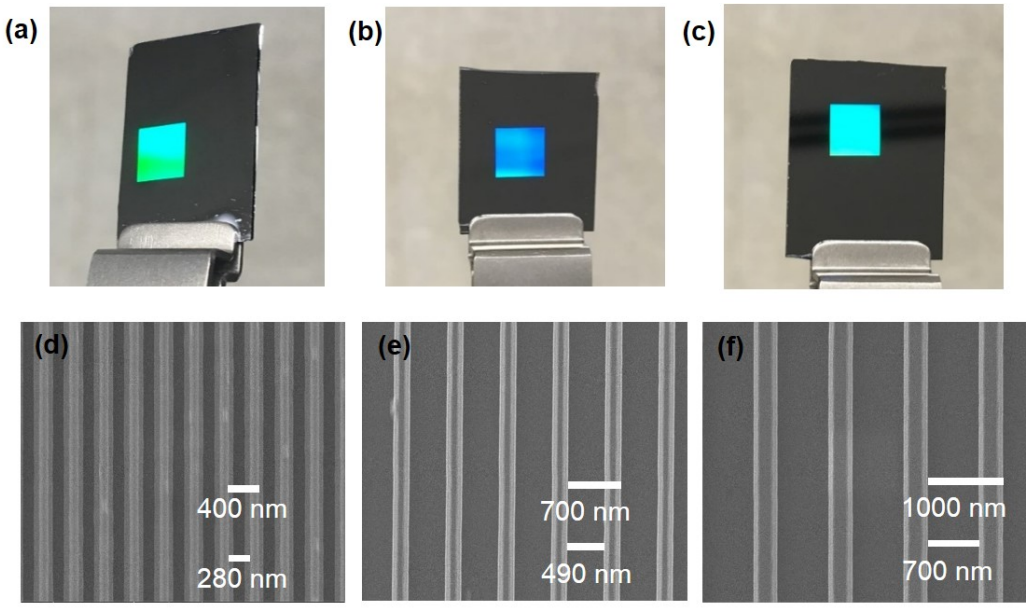

Fig. 5.1. Optical images (a-c) and SEM micrographs (d-f) of Si molds. (a, d) p = 400 nm, (b, e) p = 700 nm, and (c, f) p = 1000 nm

5.2 Au Grating Fabrication with NIL

Figure 5.2 (a-c) show the SEM micrographs of Au gratings with pitches of 400 nm, 700 nm, and 1000 nm, respectively. Grating fill factors (= width / pitch) are 700 nm for all designs. In Figure 5.2a, defects are only shown in the empty space

between Au nanowires. The defect particles were identified as Au. One of strong root causes is punch-through etching of PMMA due to thinner NIL resist at the defect locations, where the resist is unintentionally removed during the RIE. In Figure 5.2b, Au gratings of 490 nm width are peeled off from the substrate due to excessive ultrasonication during the lift-off process. Au gratings with 700 nm width and 1000 nm pitch in Figure 5.2c show residual Au debris on the edge. This failure is due to the Au deposition on the PMMA sidewall. The second Au grating layers were fabricated on the samples of $p = 400$ nm and $p = 1000$ nm. SEMs of the second Au

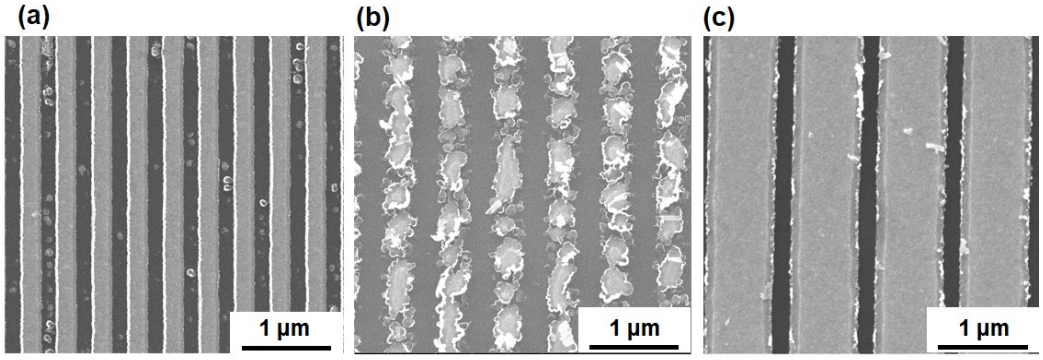

Fig. 5.2. SEM micrographs of single layer (a) $p = 400$ nm (b) $p = 700$ nm, and (c) $p = 1000$ nm

grating layer on BCB and the cross-section are shown in Figure 5.3 and Figure 5.4, respectively. As shown in Figure 5.4, the two grating layers are not perfectly aligned in this experiment.

In order to test the reproducibility, the second set of single and double-stacked gratings of $p = 400$ nm, 700 nm, and 1000 nm are also fabricated. The top-views of SEMs for the single layers and double stacked layers are shown in Figure 5.5 (a-c) and (d-f), respectively.

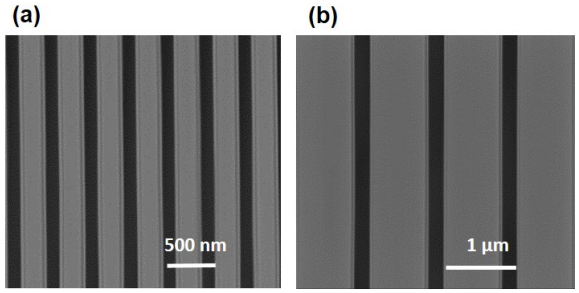

Fig. 5.3. SEM micrographs of double-stacked layer (a) $p = 400$ nm and (b) $p = 1000$ nm

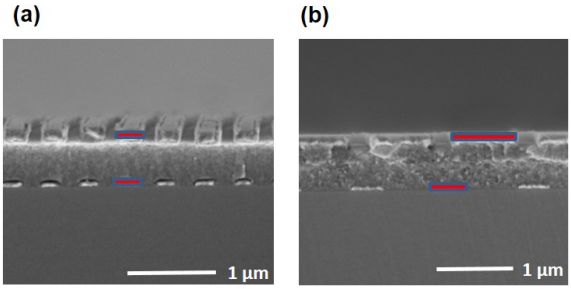

Fig. 5.4. SEM cross section micrographs of double-stacked layer (a) $p = 400$ nm and (b) $p = 1000$ nm

5.3 FTIR Measurement

5.3.1 Single Layer Transmission

TM mode transmissions of Au single grating layers with $p = 400$ nm and $p = 1000$ nm are shown in Figure 5.6a. While the general trend in the spectral transmission, the experiment results in Figure 5.6a are not as high as the predicted TM transmissions by CST simulation shown in Figure 5.6b. The plasmonic dip of Au grating with p = 1000 nm appears similar locations at 3.5 nm (experiment) and 3.4 nm (simulation). For TE transmission of the single layers of Au gratings ($p = 400$ nm and 1000 nm), the measurement data appear higher TE transmissions than the simulation (Figure 5.7). The highest TE transmissions for Au gratings of $p = 400$ nm and $p = 1000$ nm are 3.8 % and 5.8 % at 2.5 μm, respectively, while the simulation shows 0.17 % and 1.56

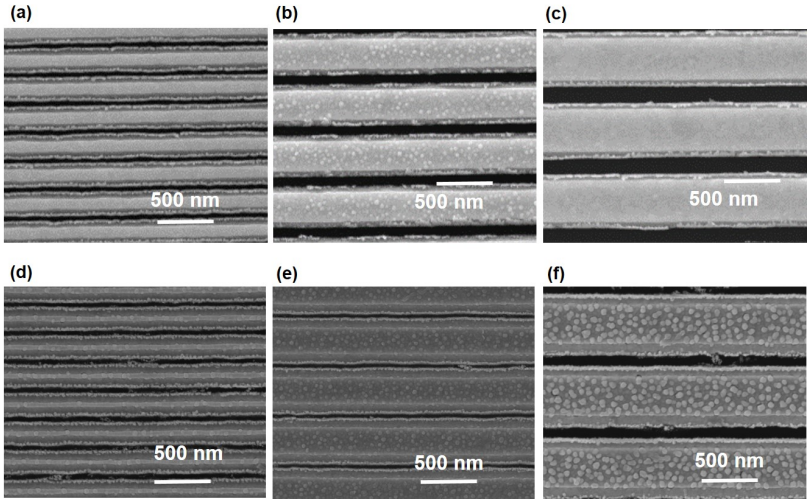

Fig. 5.5. Top view micrographs of single and double stacked layer; (a,d) $p = 400$ nm, (b,e) $p = 700$ nm, and (c,f) $p = 1000$ nm

% at 2.5 μm, respectively. TE transmission of 400 nm pitch Au grating is to decrease according to the simulation while the actual measurement shows upward trend in the wavelength from 3.7 μm to 6.0 μm. Possible reasons include the measurement error (or low signal-to-noise) in the low transmission range (< 10 %) and the fabrication imperfection as shown in Figure 5.2a.

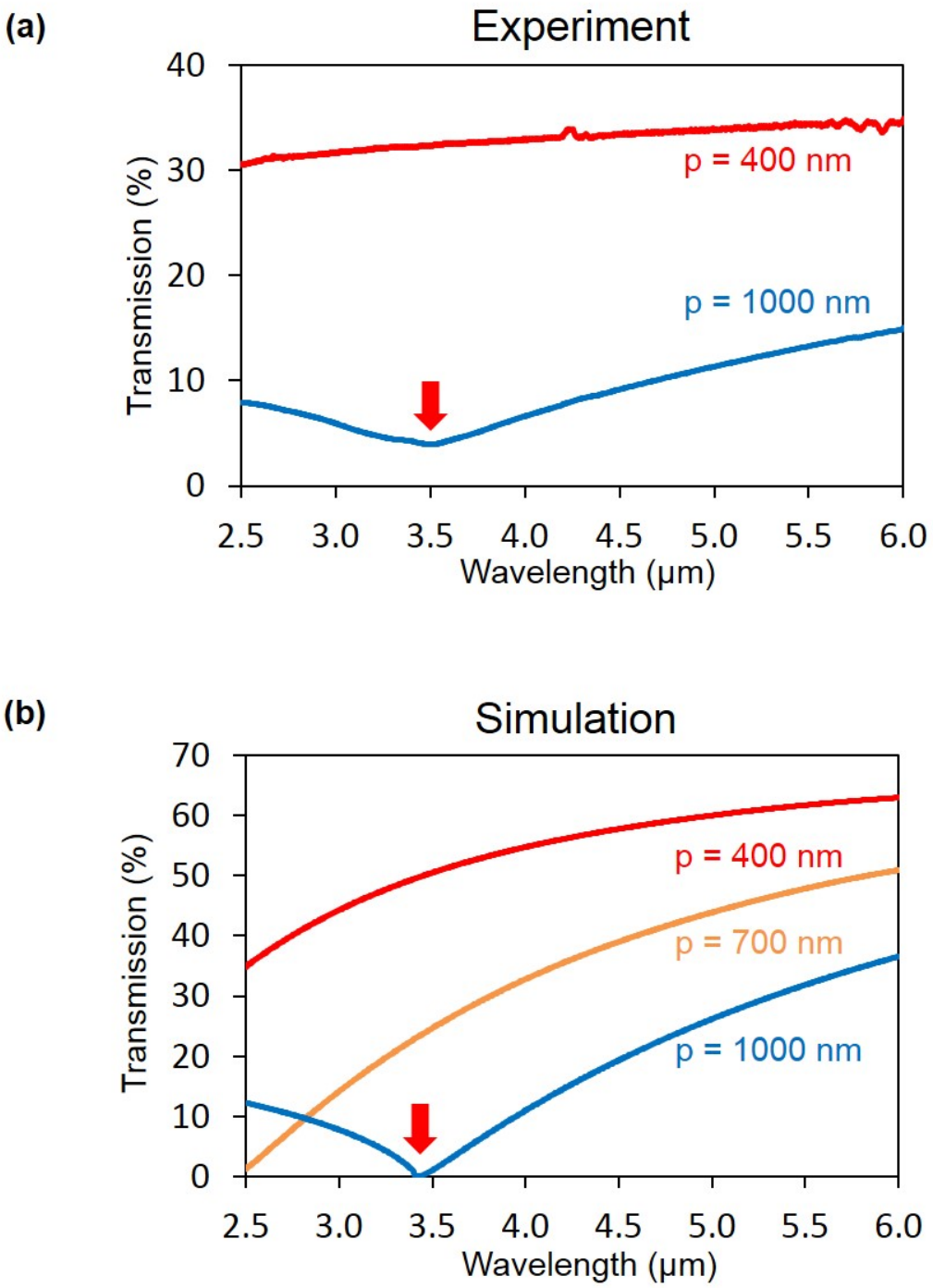

Fig. 5.6. TM transmissions of single layers. (a) Experimental result of $p = 400$ nm and $p = 1000$ nm; (b) Simulation result of $p = 400$ nm, $p = 700$ nm, and $p = 1000$ nm

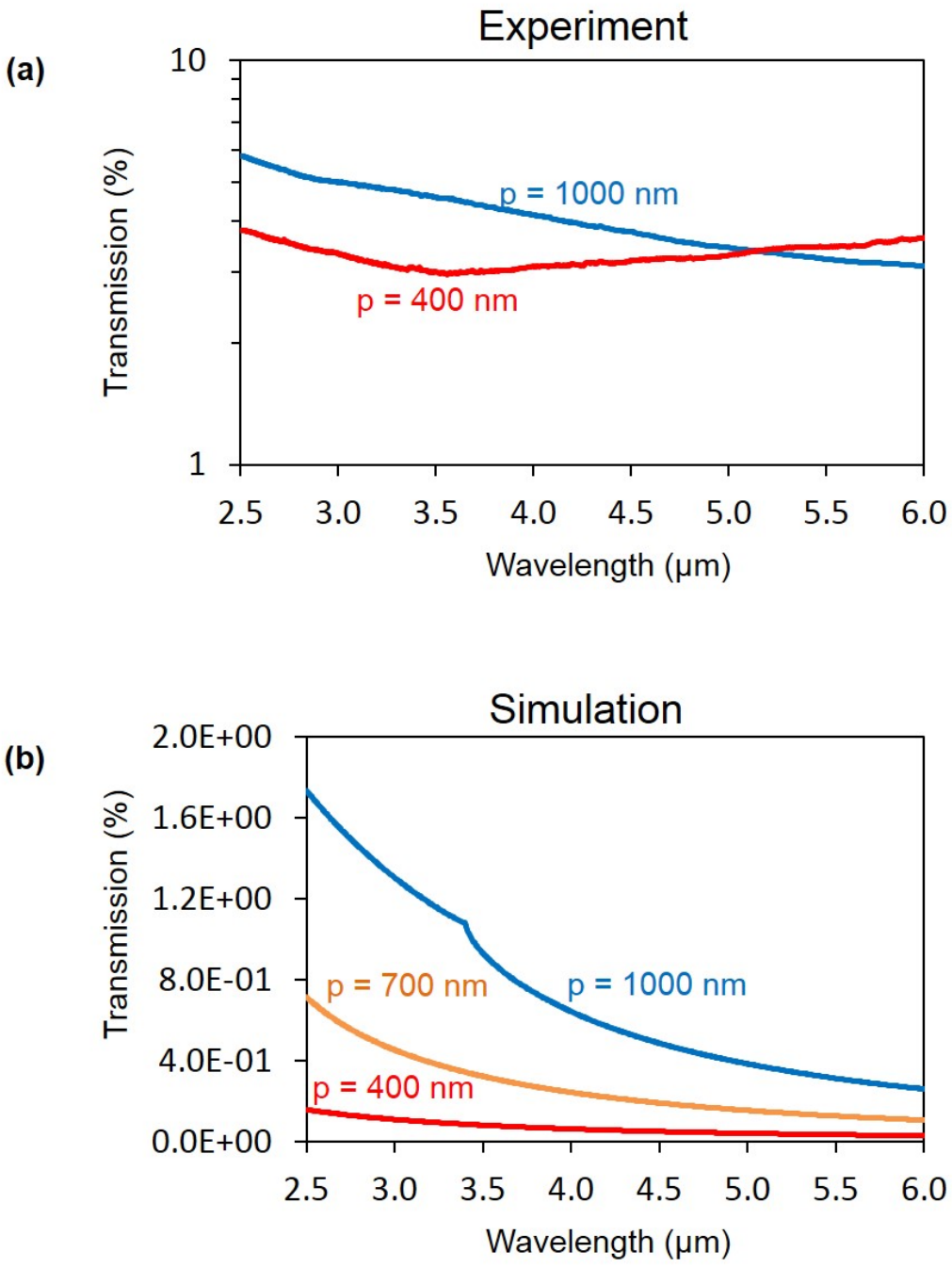

Fig. 5.7. TE transmissions of single layers. (a) Experimental result of $p = 400$ nm and $p = 1000$ nm; (b) Simulation result of $p = 400$ nm, $p = 700$ nm, and $p = 1000$ nm

5.3.2 Double Layer Transmission

TM transmissions of the double-stacked for $p = 400$ nm grating from the measurement and simulation are compared with the single layer results in Figure 5.8. The experimental data (Figure 5.8a) shows the maximum 56.1 % of transmission at 5.0 μm while the simulation shows 90.5 % of transmission at 4.4 μm (Figure 5.8b). Compared to the single layer, the double-stacked layers show 150 % improved maximum TM transmission in the experiment (Figure 5.8a). TE transmissions of the double-stacked for $p = 400$ nm grating from the measurement and simulation are compared with the single layer results in Figure 5.9. Stacking of grating layer lowers the TE transmission (Figure 5.9a) as predicted by the simulation shown in Figure 5.9b. TM transmissions of the double-stacked and single gratings of $p = 1000$ nm are shown in Figure 5.10. The simulation in Figure 5.10b shows that TM transmission of double-stacked grating grows steeply near the plasmonic dip (3.4 nm). However, the experimental result of double-stacked grating (Figure 5.10a) shows even lower transmission than the single grating in the long IR wavelength (> 4.5 μm). Various factors can cause that discrepancy including fabrication imperfection, and mismatch of material properties in simulation and experiment. Experimental and simulation of TE transmissions for single and double-stacked gratings of $p = 1000$ nm are shown in Figure 5.11a and b, respectively.

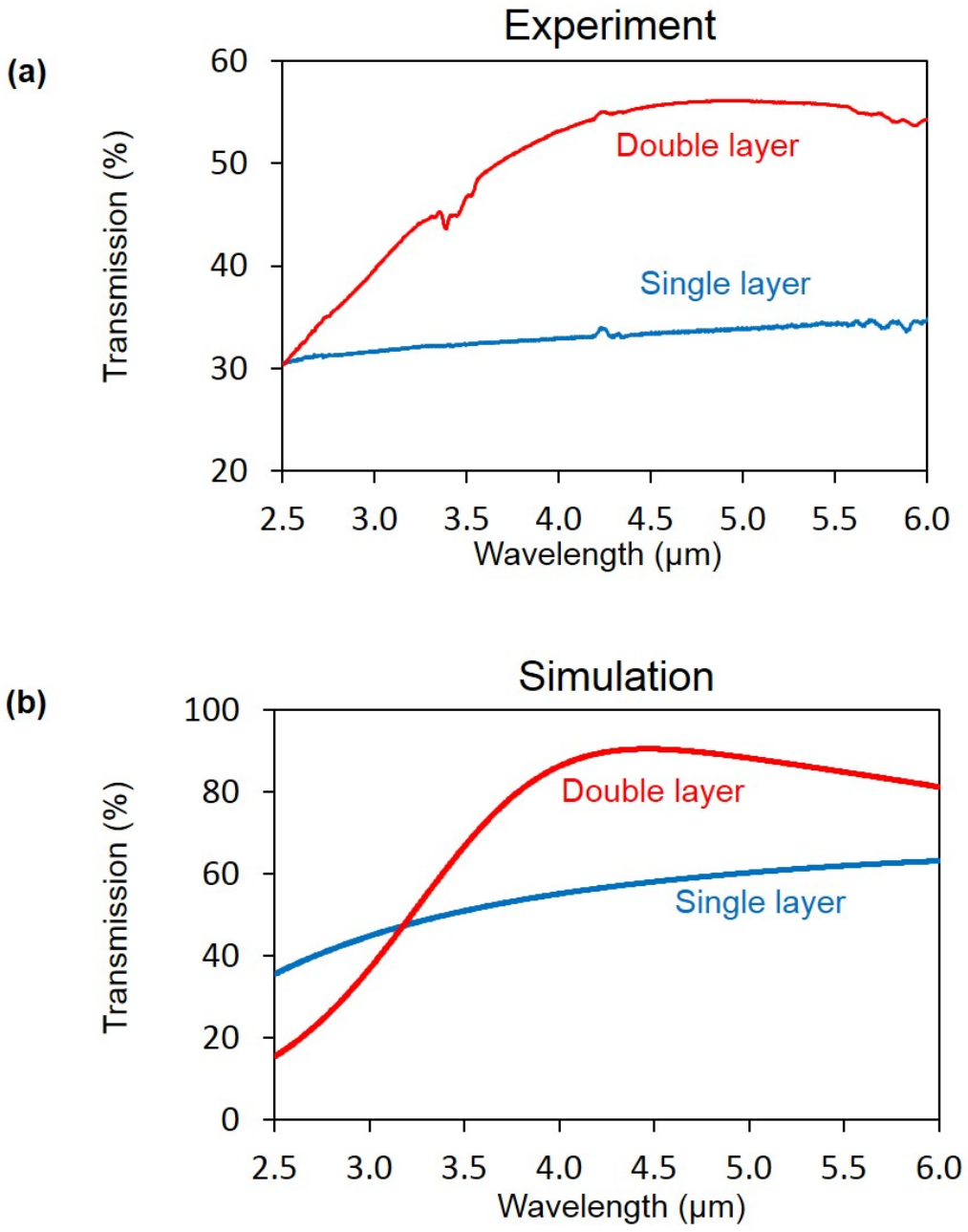

Fig. 5.8. TM transmissions of single and double-stacked layers. (a) Experimental result of $p = 400$ nm and (b) Simulation result of $p = 400$ nm

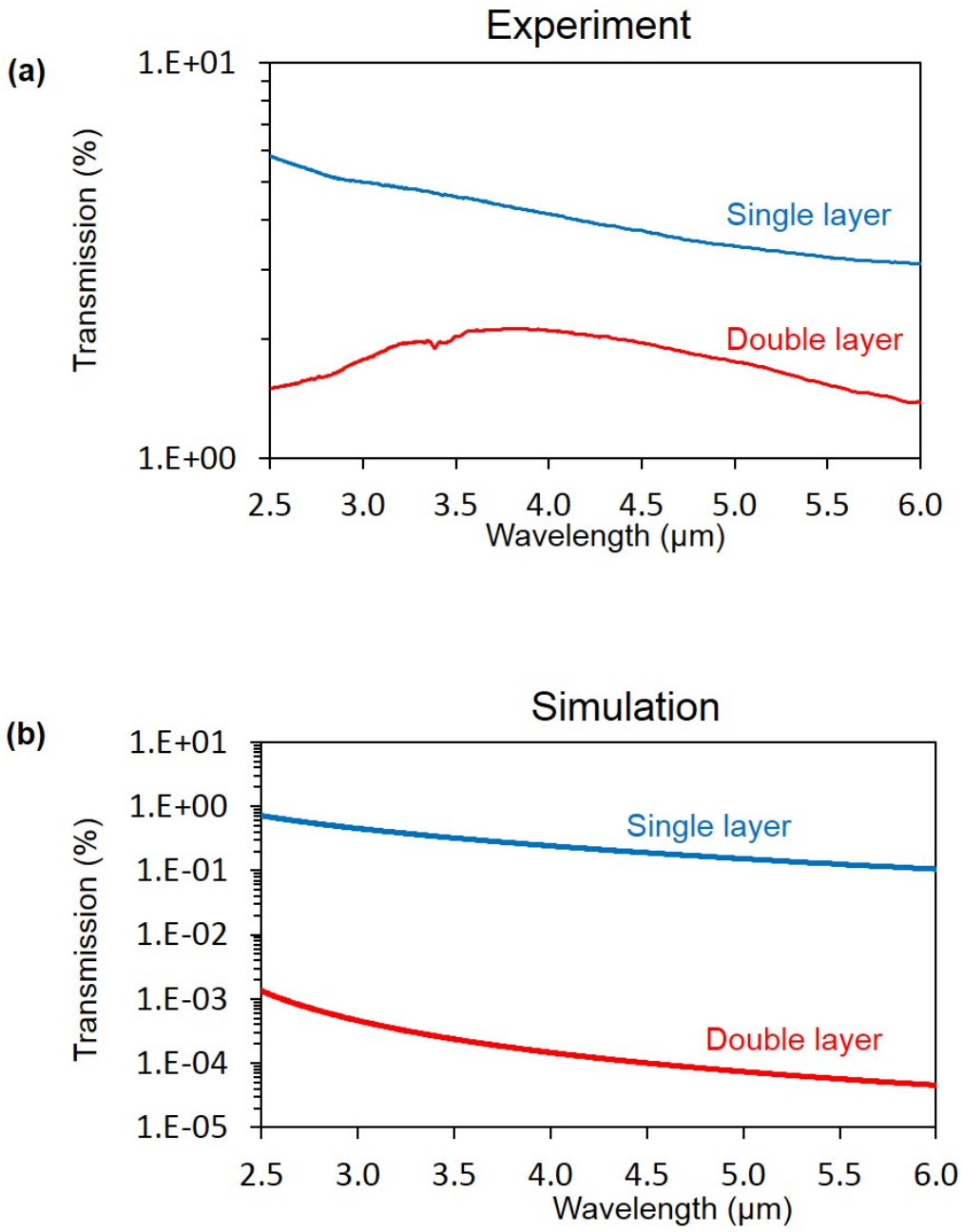

Fig. 5.9. TE transmissions of single and double-stacked layers. (a) Experimental result of $p = 400$ nm and (b) Simulation result of $p = 400$ nm

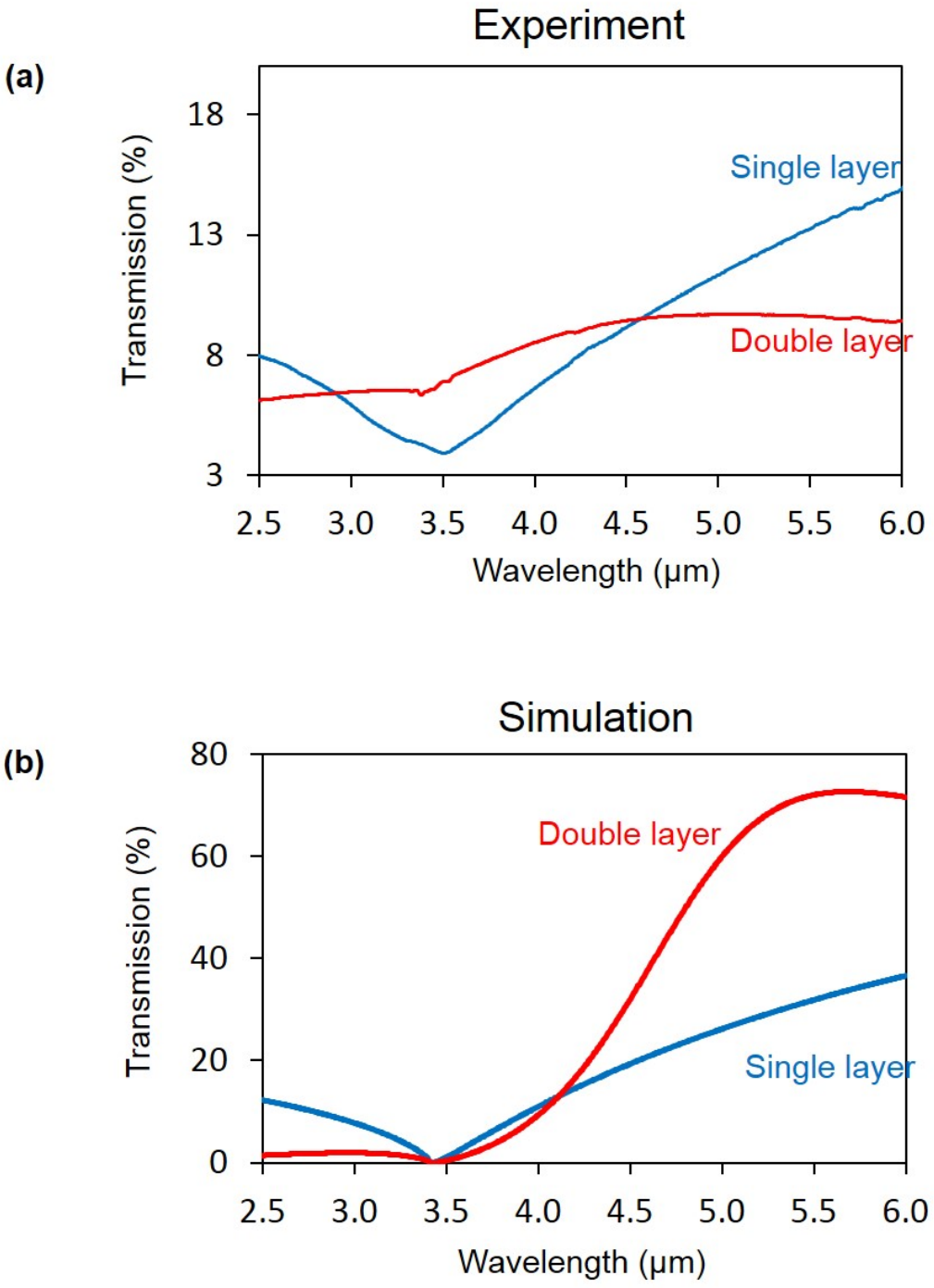

Fig. 5.10. TM transmissions of single and double-stacked layers. (a) Experimental result of $p = 1000$ nm and (b) Simulation result of $p = 1000$ nm

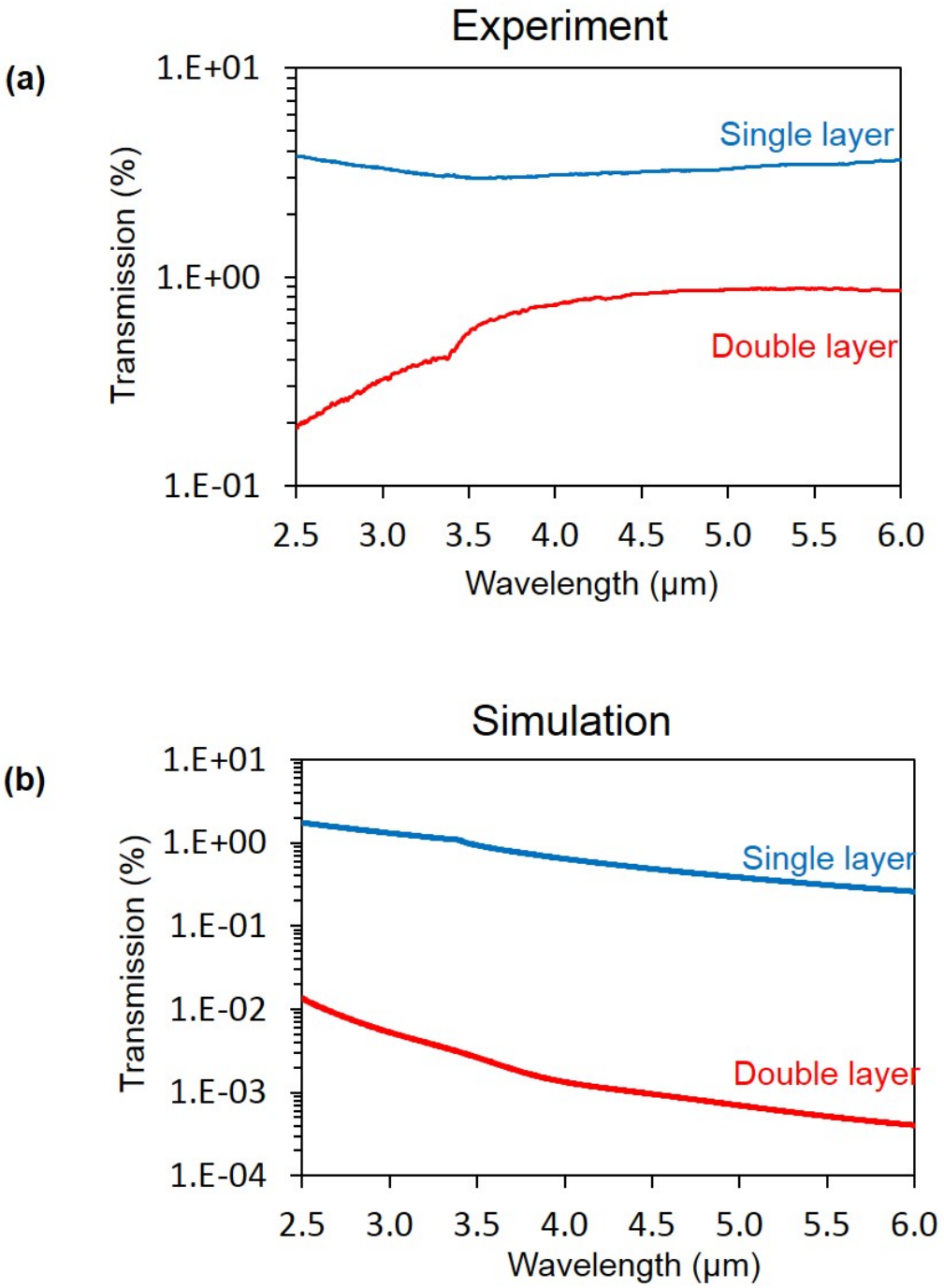

Fig. 5.11. TE transmissions of single and double-stacked layers. (a) Experimental result of $p = 1000$ nm and (b) Simulation result of $p = 1000$ nm

5.3.3 Single and Double Layer Extinction Ratio

Extinction ratio of single and double-stacked Au gratings of $p = 400$ nm are shown in Figure 5.12. Double-stacked Au grating improves the extinction ratio from 11.4 to 31.2, which are the maximum at $\lambda = 6.0\ \mu m$ (Figure 5.12a). However, the simulation shows much larger increase from 10^2 to 10^6 (Figure 5.12b).

Figure 5.13 (a and b) show extinction ratio of single and double-stacked Au gratings of $p = 1000$ nm. The plasmonic dip at 3.4 μm shown in the simulation (Figure 5.13b) does not appear in the experimental characterization (Figure 5.13a). However, the experiment confirms that the extinction ratio can be enhanced by stacking a grating with the dielectric spacer (BCB) as shown in Figure 5.13a.

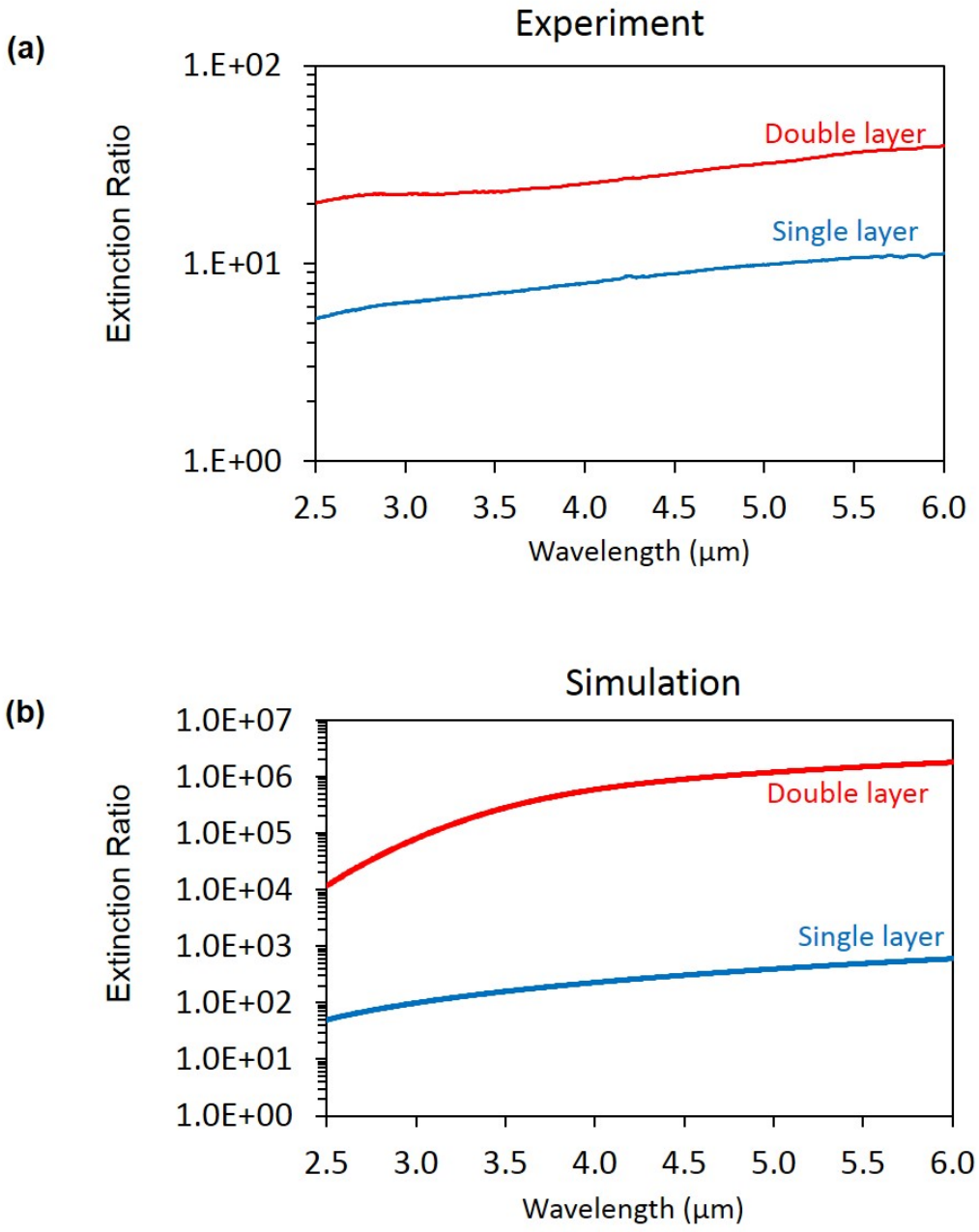

Fig. 5.12. Extinction ratio of single and double-stacked layers. (a) Experimental result of $p = 400$ nm and (b) Simulation result of $p = 400$ nm

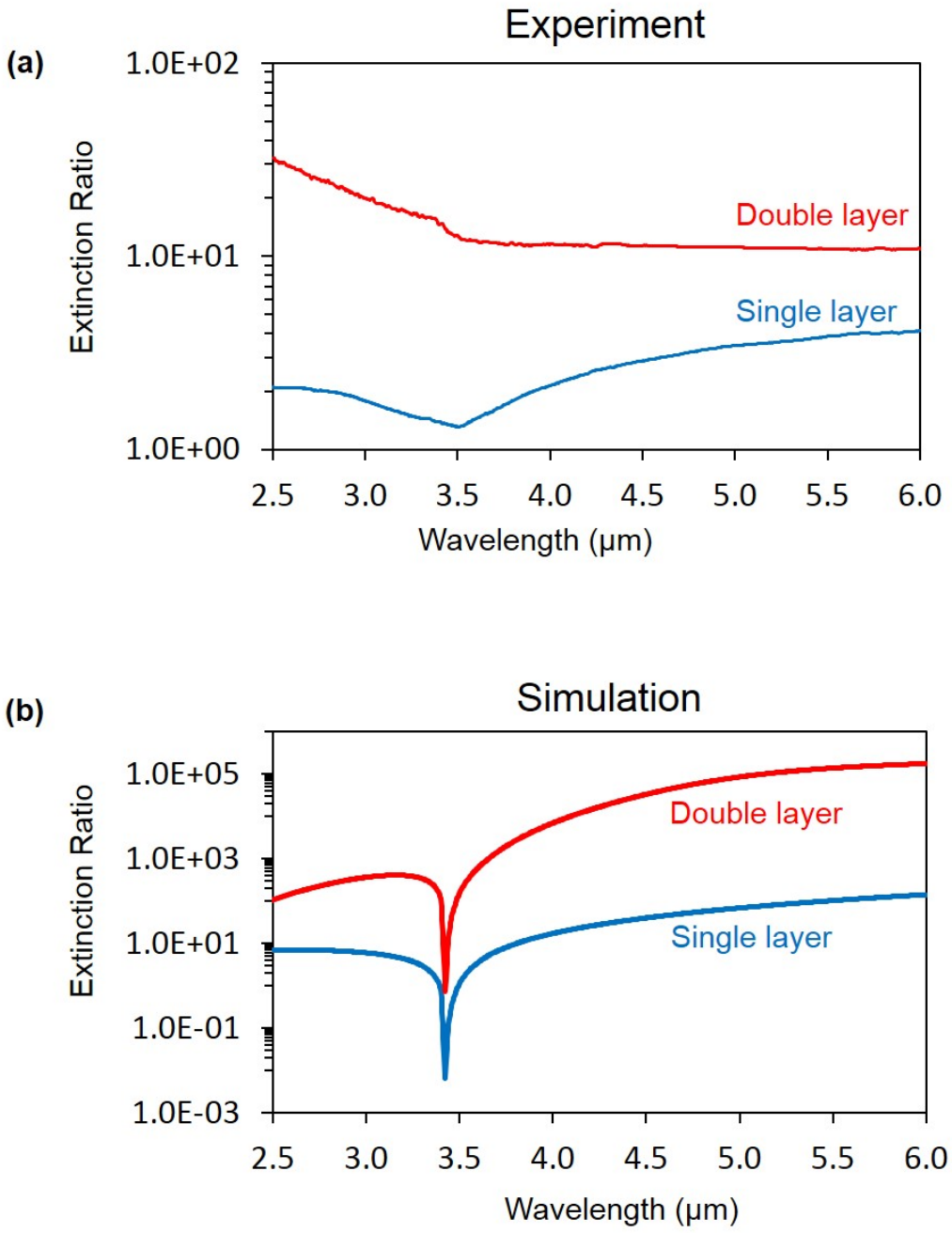

Fig. 5.13. Extinction ratio of single and double-stacked layers. (a) Experimental result of $p = 1000$ nm and (b) Simulation result of $p = 1000$ nm

5.3.4 Reproducibility Test

In order to verify the reproducibility of fabrication developed in this study, the second set of Au grating samples were fabricated. Figure 5.14 shows the TM transmission of (a) single and (b) double-stacked gratings of p = 400 nm, 700 nm, and 1000 nm. TE transmissions for single and double-stacked gratings of those pitches are shown in Figure 5.15 (a) and (b), respectively. In those experiments, however, the results failed to show enhanced TM transmission (Figure 5.14) and suppressed TE transmission (Figure 5.15). Therefore, the resultant extinction ratio (TM transmission/TE transmission) does not show significant difference between the single and double-stacked gratings as shown in Figure 5.16 (a) and (b).

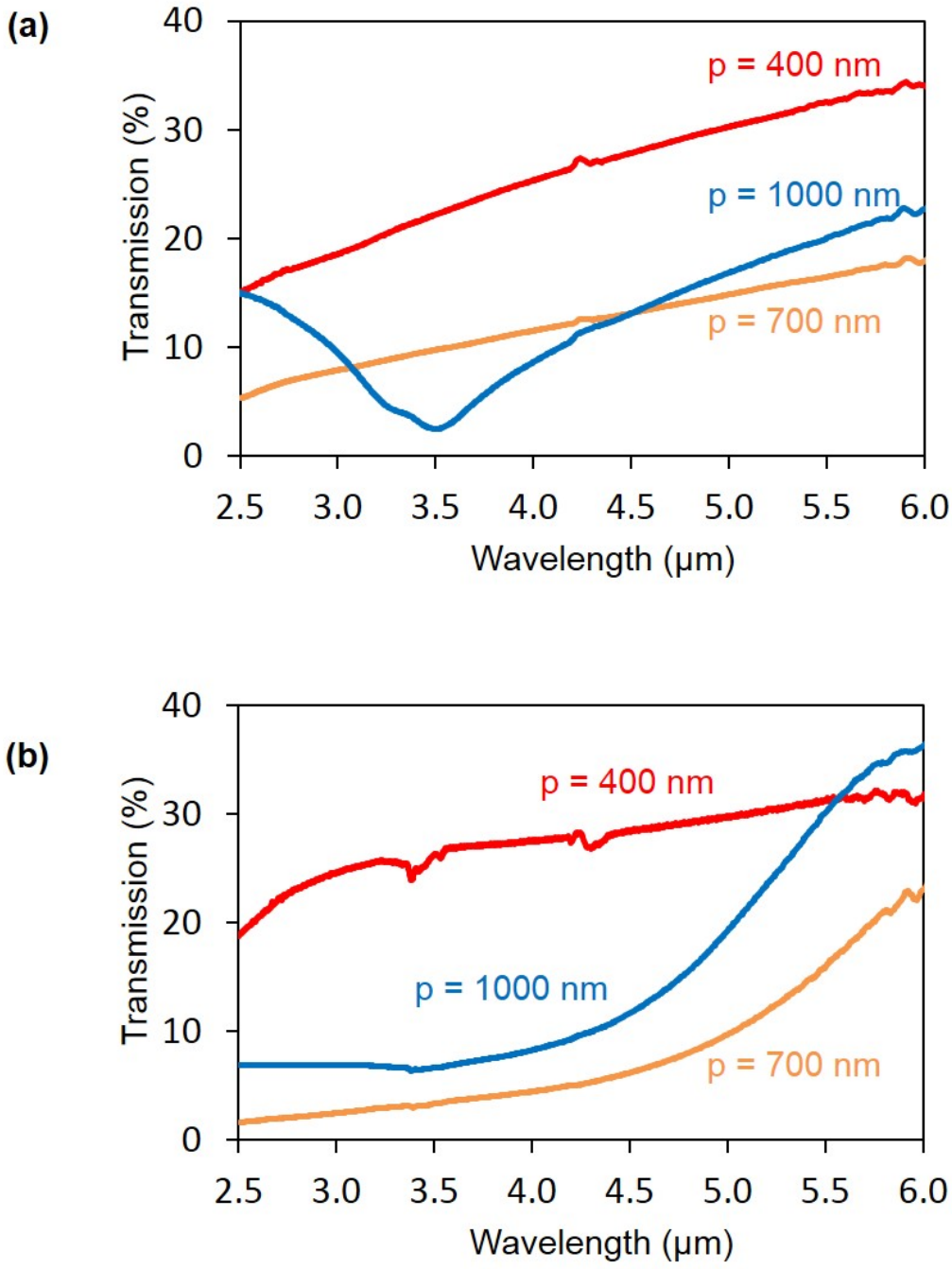

Fig. 5.14. TM transmissions of second set single layer and double-stacked layer. (a) Single layer result of $p = 400$ nm, $p = 700$ nm, and $p = 1000$ nm; (b) Double layer result of $p = 400$ nm, $p = 700$ nm, and $p = 1000$ nm

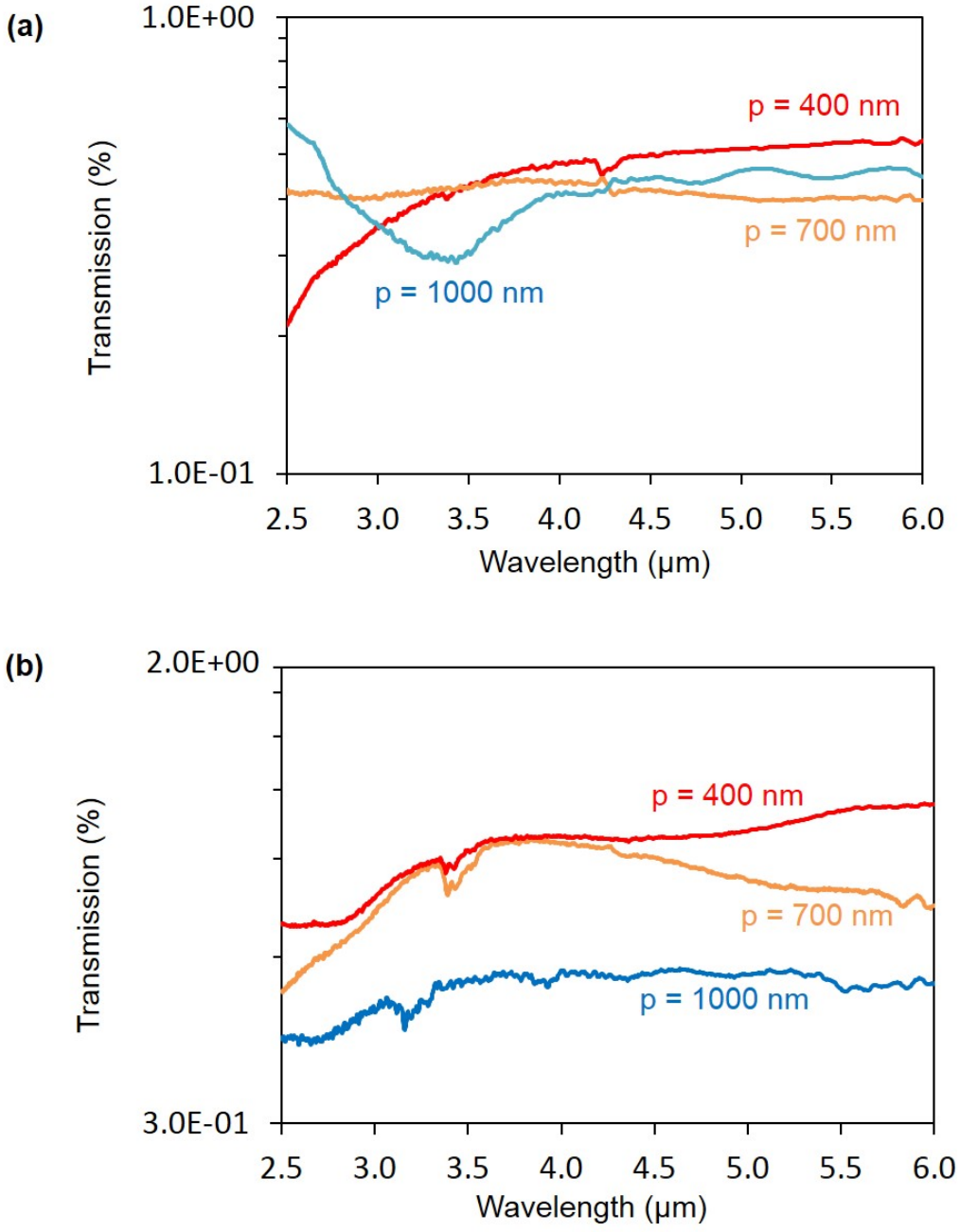

Fig. 5.15. TE transmissions of second set single layer and double-stacked layer. (a) Single layer result of $p = 400$ nm, $p = 700$ nm, and $p = 1000$ nm; (b) Double-stacked layer result of $p = 400$ nm, $p = 700$ nm, and $p = 1000$ nm

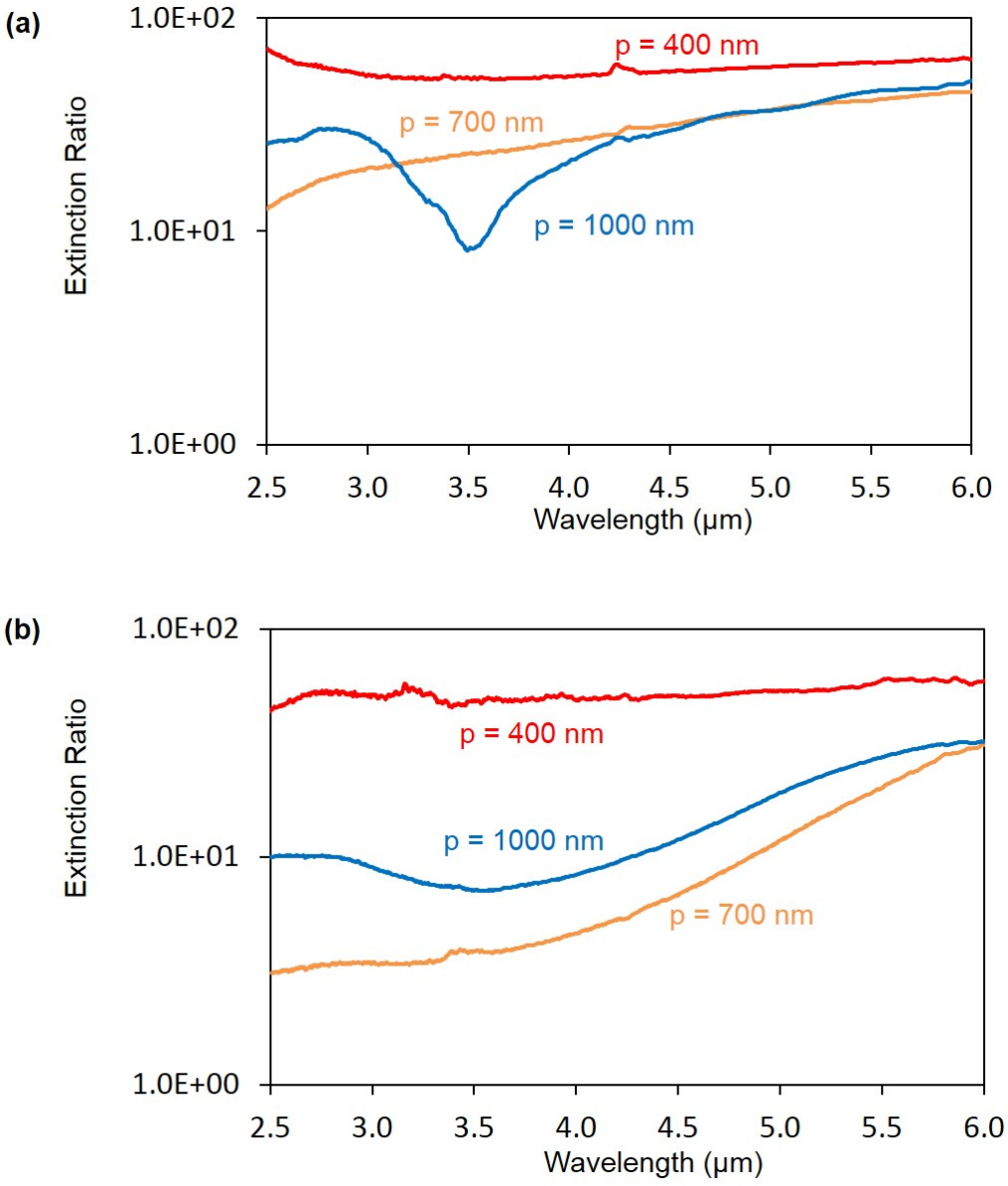

Fig. 5.16. Extinction ratio of second set single layer and double-stacked layer. (a) Single layer result of $p = 400$ nm, $p = 700$ nm, and $p = 1000$ nm; (b) Double-stacked layer result of $p = 400$ nm, $p = 700$ nm, and $p = 1000$ nm

6. CONCLUSION

6.1 Conclusion

In this MS thesis research, we tested the single and double-stacked Au gratings with a dielectric spacer to enhance the extinction ratio of IR polarimetry in mid-IR wavelength range. The results of this thesis work is summarized in Table 6.1.

Table 6.1
Extinction ratio summary

Single layer extinction ratio

Experiment		Simulation	
Pitch	Extinction ratio (1^{st}/ 2^{nd})	Pitch	Extinction ratio
400 nm	11.3 / 71.4	400 nm	2290
700 nm	NA / 46.4	700 nm	484
1000 nm	4.13 / 51.9	1000 nm	141

Double layer extinction ratio

Experiment		Simulation	
Pitch	Extinction ratio (1^{st}/ 2^{nd})	Pitch	Extinction ratio
400 nm	39.4 / 59.6	400 nm	1.79E06
700 nm	NA / 32.2	700 nm	1.79E06
1000 nm	11.0 / 32.4	1000 nm	1.77E05

6.2 Future Plans

We suggest the following research for future study:

- Improvement of nano-grating fabrication for reproducibility
- Influence of misalignment of stacked layers
- Influence of number of stacked layers
- Effect of unequal grating dimensions in the different layers

LIST OF REFERENCES

LIST OF REFERENCES

[1] L. Hutchinson, "Imaging: digital infrared breast scan shows promise for detecting cancer," *Nature Reviews Clinical Oncology*, vol. 7, no. 9, pp. 483–483, 2010.

[2] A. Rogalski, J. Antoszewski, and L. Faraone, "Third-generation infrared photodetector arrays," *Journal of Applied Physics*, vol. 105, no. 9, p. 091101, 2009.

[3] E. S. Barr, "The infrared pioneersi. sir william herschel," *Infrared Physics*, vol. 1, no. 1, pp. 1IN13IN3–2IN24IN6, 1961.

[4] S. J. Lee, Z. Ku, A. Barve, J. Montoya, W.-Y. Jang, S. Brueck, M. Sundaram, A. Reisinger, S. Krishna, and S. K. Noh, "A monolithically integrated plasmonic infrared quantum dot camera," *Nature communications*, vol. 2, p. 286, 2011.

[5] J. S. Tyo, D. L. Goldstein, D. B. Chenault, and J. A. Shaw, "Review of passive imaging polarimetry for remote sensing applications," *Applied optics*, vol. 45, no. 22, pp. 5453–5469, 2006.

[6] M. Sarkar, D. S. S. Bello, C. van Hoof, and A. J. Theuwissen, "Biologically inspired cmos image sensor for fast motion and polarization detection," *IEEE Sensors Journal*, vol. 13, no. 3, pp. 1065–1073, 2013.

[7] K. P. Gurton, A. J. Yuffa, and G. W. Videen, "Enhanced facial recognition for thermal imagery using polarimetric imaging," *Optics letters*, vol. 39, no. 13, pp. 3857–3859, 2014.

[8] *Polaris Sensor Technologies, Inc.* http://www.polarissensor.com/etherm.html. Accessed: 2016-06-20.

[9] S. Kemme, A. Cruz-Cabrera, R. Nandy, R. Boye, J. Wendt, T. Carter, and S. Samora, "Micropolarizer arrays in the mwir for snapshot polarimetric imaging," in *Defense and Security Symposium*, pp. 655604–11, International Society for Optics and Photonics.

[10] J. Vaillancourt and X. Lu, "A monolithically integrated multi-spectral polarimetric quantum dot infrared photodetector," in *SPIE OPTO: Integrated Optoelectronic Devices*, p. 722216, International Society for Optics and Photonics, 2009.

[11] M. Kulkarni and V. Gruev, "Integrated spectral-polarization imaging sensor with aluminum nanowire polarization filters," *Optics express*, vol. 20, no. 21, pp. 22997–23012, 2012.

[12] Q. Li, Z. Li, N. Li, X. Chen, P. Chen, X. Shen, and W. Lu, "High-polarization-discriminating infrared detection using a single quantum well sandwiched in plasmonic micro-cavity," *Scientific reports*, vol. 4, 2014.

[13] E. Hecht, *Optics 4th edition*. Addison Wesley Longman Inc, pp. 325-329, 1998.

[14] C.-C. Chang, Y. D. Sharma, Y.-S. Kim, J. A. Bur, R. V. Shenoi, S. Krishna, D. Huang, and S.-Y. Lin, "A surface plasmon enhanced infrared photodetector based on inas quantum dots," *Nano letters*, vol. 10, no. 5, pp. 1704–1709, 2010.

[15] W. L. Barnes, A. Dereux, and T. W. Ebbesen, "Surface plasmon subwavelength optics," *Nature*, vol. 424, no. 6950, pp. 824–830, 2003.

[16] L. J. Guo, "Recent progress in nanoimprint technology and its applications," *Journal of Physics D: Applied Physics*, vol. 37, no. 11, p. R123, 2004.